Association Euratom - Risø National Laboratory annual progress report 1999

Lynov, Jens-Peter; Singh, Bachu Narain

Publication date:
2001

Document Version
Publisher's PDF, also known as Version of record

Association Euratom - Risø National Laboratory Annual Progress Report 1999

Edited by J.P. Lynov and B.N. Singh

Abstract The programme of the Research Unit of the Fusion Association Euratom - Risø National Laboratory covers work in fusion plasma physics and in fusion technology. The fusion plasma physics group has activities within development of laser diagnostics for fusion plasmas and studies of nonlinear dynamical processes related to electrostatic turbulence and turbulent transport in magnetised plasmas. The activities in technology cover investigations of radiation damage of fusion reactor materials. These activities contribute to the Next Step, the Long-term and the Underlying Fusion Technology programme. A summary is presented of the results obtained in the Research Unit during 1999.

ISBN 87-550-2834-9
ISBN 87-550-2835-7 (Internet)
ISSN 0106-2840

Print: Danka Services International A/S, 2001

Contents

3. Fusion Technology 30

1. Research Unit

The activities in the Research Unit cover two main areas:

Fusion Plasma Physics which includes:

- *Laser plasma diagnostics*. Development of laser diagnostics for spatially localised turbulence measurements. In collaboration with IPP Garching measurements are being performed on the W7-AS stellarator with a collective scattering diagnostic.
- *Nonlinear dynamics of fusion plasmas*. For the interpretation of the results from the laser diagnostic, extensive computer simulations are carried out of the plasma density fluctuations under various types of electrostatic turbulence. These simulations are also used for studies of nonlinear plasma processes of relevance to turbulent transport.

Fusion Technology which includes:

- Experimental and theoretical investigations of the effects of irradiation on the microstructural evolution and on the physical and mechanical properties of metals and alloys relevant to the Next Step, the Long Term and Underlying Fusion Technology Programme.

The **global indicators** for the Research Unit in 1999 are:

• Professional staff	13.7	man-years
• Support staff	4.9	man-years
• Total expenditure - incl. mobility	2.77	MioEuro
• Total Euratom support	0.78	MioEuro

2. Fusion Plasma Physics

2.1 Introduction

The activities in this area have been carried out under the Plasma Physics and Fluid Dynamics Programme in the Optics and Fluid Dynamics Department. The main objective of the research is to contribute to the understanding of turbulent transport in fusion plasmas. In the work towards this objective, the programme interacts with other activities in the department in the fields of optics and fluid dynamics to the mutual scientific benefit of the projects involved.

The main results obtained during 1999 can be summarised as follows:
In collaboration with the Max-Planck-Institute for Plasma Physics in Garching, Germany, a number of successful measurements have been carried out with Risø's laser diagnostic on the Wendelstein 7-AS stellarator. Two different methods to obtain localized measurements of turbulence have been tested with good results. The first method was originally developed by the ALTAIR team at TORE SUPRA, while the second is a new method developed by us. The experimental studies were supported by a number of theoretical and numerical studies. Fully three-dimensional simulations of plasma turbulence in realistic machine geometries have been carried out, and effects of magnetic field geometry and of plasma boundary conditions have been investigated. Numerical simulations were used with good results to test predictions from the Turbulent Equipartion Model and these simulations demonstrated the intermittent dynamical behaviour of transport barriers in the plasma.

In this report, a brief description is included of three special projects, which are derived from the main scientific programme. These projects are: 1) pellet injectors and 2) industrial spin-off of laser anemometers for wind turbines and 3) lectures in plasma physics.

2.2 Laser Plasma Diagnostics

2.2.1 The LOTUS density fluctuation diagnostic

N.P. Basse, M. Saffman (Department of Physics, University of Wisconsin, USA), *S. Zoletnik (CAT-Science, Budapest, Hungary)*, *M. Endler (Max-Planck-Institut für Plasmaphysik, Teilinstitut Greifswald, Germany) , B.O. Sass, J.C. Thorsen and H.E. Larsen*

2.2.1.1 Introduction

On the W7-AS (**W**endelstein **7**-**A**dvanced **S**tellarator) at IPP-Garching, the Department of Optics and Fluid Dynamics has in 1996 installed a CO_2 laser based collective scattering diagnostic recently dubbed LOTUS (**Lo**calised **Tu**rbulence **S**cattering) [1]. This augments the already existing density fluctuation diagnostics such as the Li-beam and reflectometry.

The chapter is organised as follows: Section 2 describes the optical set-up at W7-AS and introduces fundamental quantities. In section 3 we present results of the 'traditional' method of localisation as developed by the ALTAIR (**A**nalyse **L**ocalisée du **T**ransport **A**normal par **I**nfra **R**ouge) team at TORE SUPRA [2]. Section 4 describes results from our novel two-point correlation technique also leading to spatial localisation [3]. In section 5 we discuss

wavenumber scans. Section 6 is devoted to an H*-mode case study [4]. Finally, we state some conclusions in section 7.

2.2.1.2 Optical set-up

W7-AS is a five field period device with a pentagon-like shape [5]. The toroidal angle φ is defined to be 0^o at the module centers and ± 36^o at the module borders. The plasma shape is roughly triangular at 0^o, elliptic at ± 36^o. The LOTUS diagnostic is positioned at 29.14^o, where the flux surfaces are close to elliptic but with a tilt of the major radius with respect to vertical.

Figure 1 shows the basic optical setup of the diagnostic. The M (**m**ain) CO_2 laser beam represented by the thick red line is split into two parts in the Bragg cell. The M beam remains unchanged with slightly decreased intensity while another beam – the LO (**l**ocal **o**scillator) beam is created. The LO beam is frequency shifted 40 MHz with respect to the M beam. The two beams are then each split in two by a diffractive beam splitter and are focused into the plasma. The region where the two pairs of LO and M beams cross is the measurement volume, i.e. the region wherefrom one observes a scattered signal. The crossing angle between the beams θ_s defines the measured wavenumber according to $k_{pol} \sim k_{laser}\ \theta_s$, where $k_{laser} = 2\pi/\lambda_{laser} =$ 5933 cm^{-1}. We write k_{pol} instead of $k_\perp$ because our measurement volumes are passing close to the plasma center so the contribution from the radial component of the fluctuation wave vector is negligible. The length of the measurement volumes is $L_{vol} \sim 4w/\theta_s$ where w is the waist (i.e. 'radius') of the beams at $z = 0$ where they are focused.

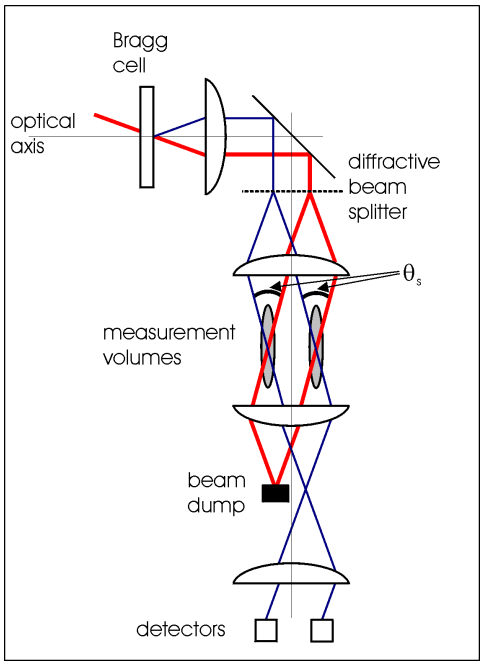

Figure 1. A sketch of the optical system. The M beam is shown as a thick red line, the LO beam as a narrow blue line. The plane defined by the crossing beams has a small angle α with respect to the (R,z)-plane (see Figure 2), so we are measuring the near-perpendicular component of the fluctuation wave vector.

Example: A typical wavenumber measured is $k_{pol} = 30$ cm^{-1}. That corresponds to an angle θ_s = 5 mrad (0.3 degrees) or $L_{vol} \sim$ 16 mm/5 mrad = 316 cm for a beam waist of 4 mm. This means that our measurement is line integrated along the vertical volumes.

The signals detected are centered at 40 MHz and are then downshifted to be centered at 0 Hz. A signal arises around 0 Hz due to parasitic scattering of the M into the LO beams, this is called the ’40 MHz leak’ and is purely instrumental.

Figure 2 shows the relative position of the two measurement volumes as seen from above. The ‘major radius angle’ θ_R = Arcsin($|\boldsymbol{d}_R|/|\boldsymbol{d}|$) defines the angle between the line connecting the volume centers and the toroidal direction.

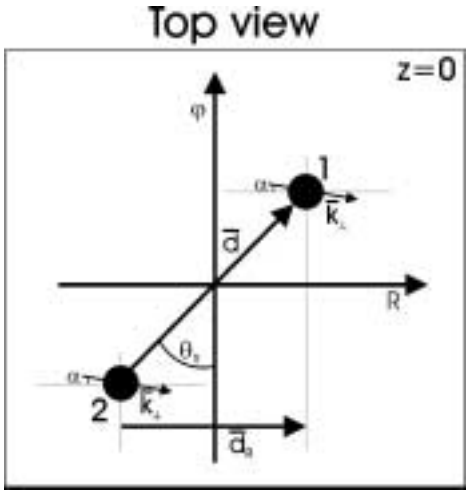

Figure 2. The relative position of the measurement volumes labelled ‘1’ and ‘2’. θ_R is variable, but the angle α of the measured wave vector with respect to the major radius does not depend on θ_R.

Figure 3 shows the geometry going into the construction of the ‘horizontal pitch angle’ $\theta_p(z)$ = Arctan($B_R(z)/B_\varphi(z)$). The fluctuation wave vector is shown as perpendicular to the magnetic field according to the assumption that $k_{\parallel} \ll k_{\perp}$.

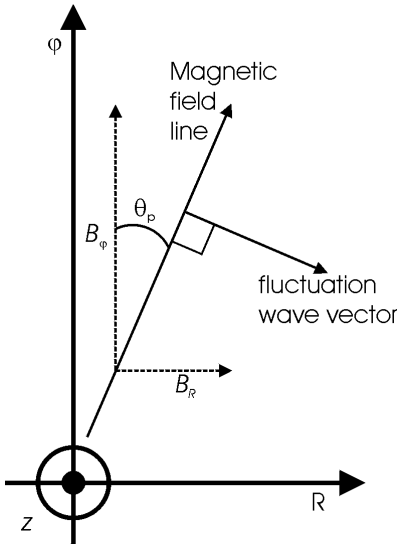

Figure 3. Definition of the horizontal pitch angle.

The last figure we need to describe the set-up is Figure 4. To the left we show flux surfaces at the toroidal angle where our diagnostic is situated. The equilibrium is calculated for ι_a = 0.344; at larger ι_a an equilibrium is not always available due to island formation. Generally,

the plasma size decreases with increasing ι_a. The vertical line shown indicates the position of the origin of Figure 2. The upper right figure shows the plasma β in percent as function of r_{eff}, the effective minor radius. Lower right figure shows θ_p as a function of z along the vertical line; the relationship is seen to be roughly linear. Combining this fact with Figure 3, we conclude that the major component of the fluctuation wave vector turns 16 degrees along the measurement volumes. This rotation is an essential point for both localisation methods discussed below.

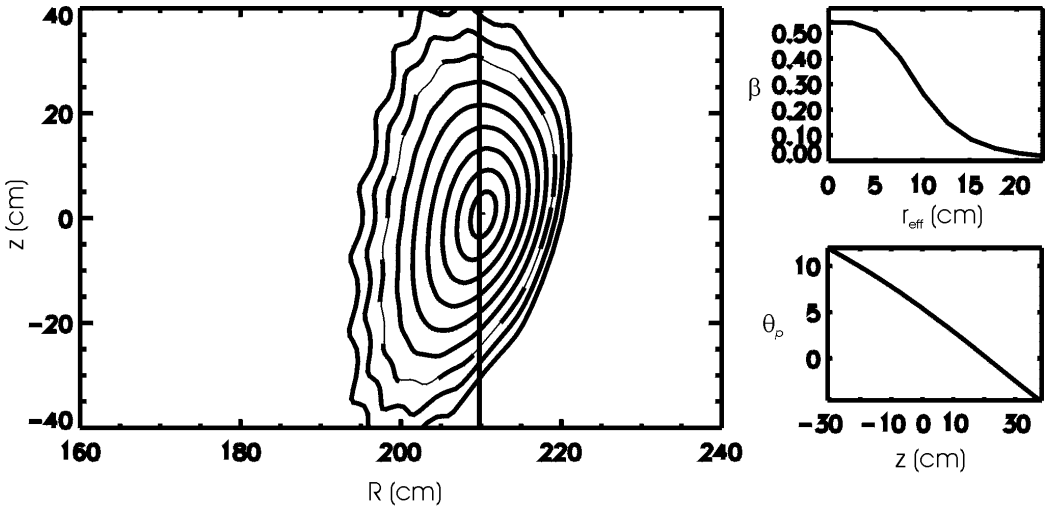

Figure 4. Flux surfaces for an $\iota_a = 0.344$ plasma at the toroidal angle $\varphi = 29.14^o$ where LOTUS is installed. The dashed line marks the LCFS (**l**ast **c**losed **f**lux **s**urface) due to limiter action.

To achieve a basic understanding of why the pitch angle variation can be utilised for localisation we write an equation for the scattered power *I(α,k)* detected for each volume of the diagnostic:

$$I(\alpha, k_\perp) = \int_{z_{bot}}^{z_{top}} dz\, \delta n^2(k_\perp z)\, e^{-((\alpha-\theta_p(z))N\pi/2)^2} \quad [2]$$

where δn is the RMS value of the density fluctuations, z_{bot} = -30 cm, z_{top} = 40 cm and $N = 2w/\lambda = k_{pol}w/\pi$ is the 'fringe number'; a measure of how many wavelengths fit into the measurement volume diameter. If N is somewhat larger than unity, the scattered power can be interpreted as the spatial Fourier transform of the density fluctuations. The exponential function is called the 'exponential selectivity function'; all quantities in the exponent are fixed along z except the pitch angle. Therefore the size of the selectivity function varies along z, so that the scattered signal originates predominantly from the region where the selectivity function is large (factor in exponent small). So we get a signal from the region where α and θ_p are parallel.

In the next two sections we will describe two set-ups both using the pitch angle variation to obtain localised density fluctuation measurements. The essential difference between the two setups is the size of the fringe number.

2.2.1.3 Wide beam localisation

We begin the presentation of measurements for the wb (**w**ide **b**eam) localisation method. As the name implies, the beams in this method have a large waist and therefore a large fringe

number. We describe measurements with k_{pol} = 15 cm^{-1}, w = 33 mm (N = 16) and variable α. For these shots we only had one volume; the volume was centered along the vertical line shown in Figure 4.

Six nearly identical discharges were made. We changed α between each shot and could thereby construct a six-point profile of the density fluctuations along the volume. The α values were 12 (bottom), 8, 6, 4, 0 and –4 (top) degrees, see Figure 5. A signal at positive frequencies is due to fluctuations moving inward parallel to R, negative frequencies due to fluctuations moving outward parallel to R. It is seen that the edge signals are larger than the center signals. The signal around 0 Hz up to about ±100 kHz is the 40 MHz leak signal.

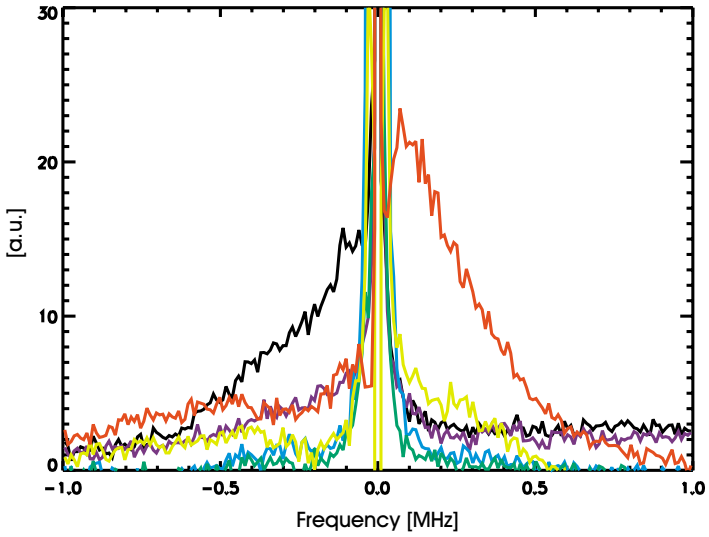

Figure 5. Overlayed power spectra for the steady-state phase (250 to 400 ms) of the 6 shots. Bottom to top of plasma: Black/dark blue/light blue/green/yellow/red.

The colour plots in Figure 6 shows the scattered power for the intervals [-200,-100] kHz (left) and [100,200] kHz (right) vs. time and 'vertical position'; a vertical position –1 is the bottom plasma, 0 is central plasma and 1 is top plasma. We see large signals in the plasma startup phase (0 to 250 ms), then the plasma quiets down and stays quiescent for 150 ms until 400 ms. In this phase it is seen that the bottom signal dominates for negative frequencies and the top dominates for positive frequencies. This is interpreted as poloidally moving structures detected both at the top and bottom edges of the plasma and moving in the ion diamagnetic drift direction outside the LCFS. At higher frequencies the direction of the fluctuations is reversed; they propagate in the electron diamagnetic drift direction inside the LCFS. This reversal is thought to be due to the inversion of the radial electric field which takes place close to the LCFS [6].

From 400 to 600 ms an ohmic plasma current is driven through the plasma, see top traces in Figure 6. The plasma current increases the rotational transform from the initial value 0.344 to a larger value, thereby passing the ι_a = 0.35 'edge' of W7-AS [7] and dropping into a bad confinement regime. This is clearly observed as a drop in the stored energy and an increase of the particle fuelling to maintain constant density. The plasma re-stabilises after the current is returned to zero. It is interesting to see that the fluctuation signature in response to the confinement change resembles the start-up feature, the plasma has to 'restart' after the factor 2 confinement degradation. We consider the study of these current ramping experiments as very important; the change of stored energy is much larger than what one observes in for example

an L-H* transition where one typically achieves a 20 to 30% increase of stored energy, not the doubling observed in tokamaks.

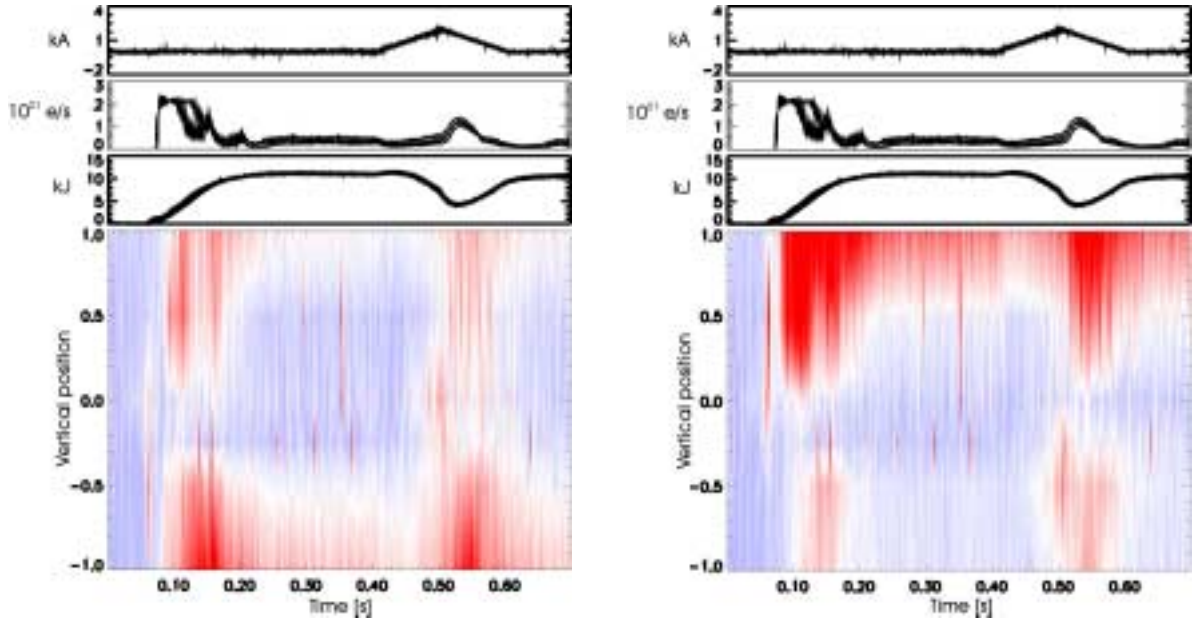

Figure 6. From top to bottom: The plasma current in kA for the six discharges, the Deuterium fuelling rate and the stored energy in kJ. Lower left plot shows the scattered power from -200 to -100 kHz vs. time and vertical position, lower right plot shows the scattered power from 100 to 200 kHz. Red is high power, blue low power.

To get a better handle on the spatial profile of the fluctuation power, we plot profiles in Figure 7. The left plot represents cuts through the contour plots in the quiescent phase seen in Figure 6. It is clearly seen that negative frequencies dominate in the bottom plasma and positive frequencies dominate at the top. The right plots shows the scattered power integrated over all frequencies (both positive and negative) vs. vertical position.

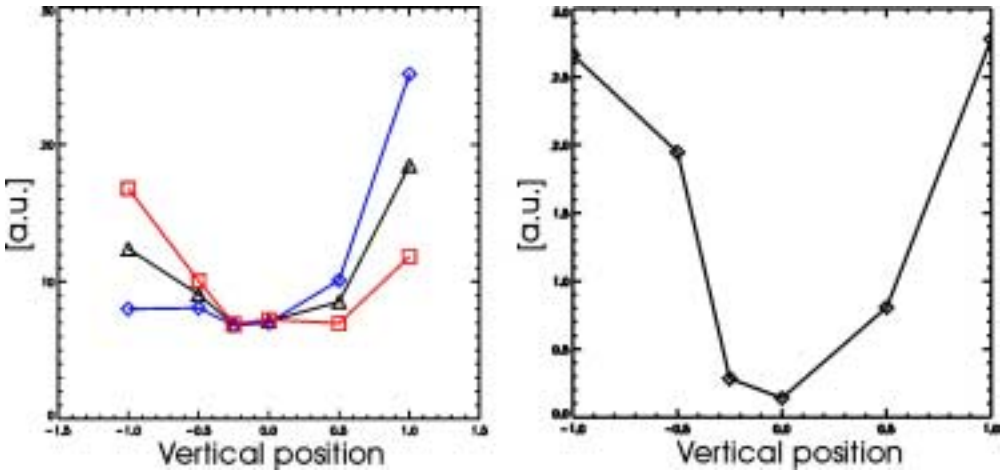

Figure 7. The left-hand figure shows the scattered power from -200 to -100 kHz (red squares), scattered power from 100 to 200 kHz (blue diamonds) and the average of these (black triangles). The right-hand figure shows the scattered power integrated over all frequencies.

2.2.1.4 Narrow beam localisation

We continue with an illustration of the nb (**n**arrow **b**eam) localisation method. The beams had a small waist and therefore a small fringe number. We describe measurements with k_{pol} = 20 cm^{-1}, w = 4 mm (N = 2.5) and fixed α. For these shots we had two volumes; the volumes could be rotated (i.e. one could change θ_R) around the vertical line shown in Figure 4.

Having such a small fringe number, localisation is impossible to obtain by changing α. But assuming that fluctuations stretch along the field lines and that the cross-field correlation length is small, we can still use the pitch angle variation to our advantage. By changing θ_R in steps between each shot, we would expect to see a crosscorrelation signal at angles where θ_R and θ_p are parallel. This constitutes a novel method of localisation [3,8].

The discharges were identical to the ones described in section 3. In Figure 8 we show three contour plots of the normalised crosspower amplitude vs. time and frequency. The colour scale shown is the amplitude from 0.1 (red) to 0.4 (black) in normalised units. It is clear that we see the same phenomena as described in section 3. $\theta_R > 0$ means that we see the signal from the lower parts of the plasma, $\theta_R < 0$ means fluctuations are observed originating in the upper regions of the plasma. The crosspower amplitude is a measure of the fluctuation amplitude.

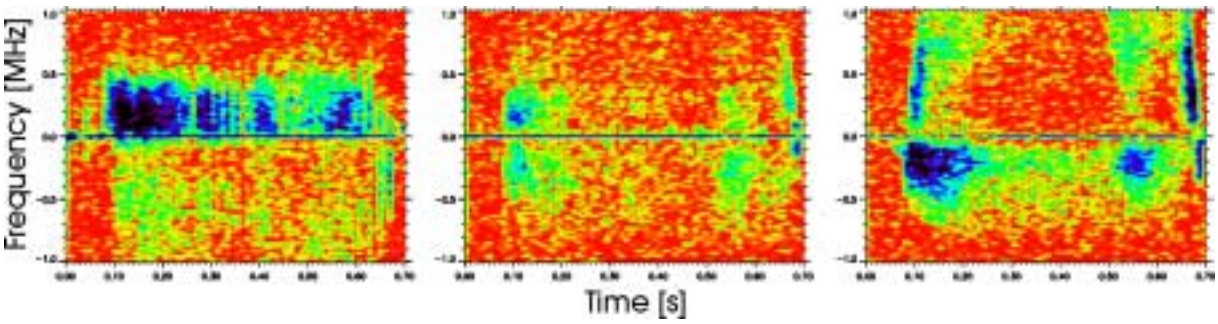

Figure 8. Normalised crosspower amplitude for θ_R = -9.5^o (left), θ_R = 0.5^o (center) and θ_R = 10.5^o (right).The angles are not calibrated to the pitch angle and should not be taken literally.

We made a series of this discharge type where θ_R was increased until the crosscorrelation disappeared. This procedure led to an estimate of the cross-field correlation length of 1 cm.

2.2.1.5 Wavenumber scans

We proceed with a short discription of 'wavenumber' scans; here, a series of identical shots were made where we changed the size of k_{pol} in steps between shots. Figure 9 shows the frequency integrated, scattered power vs. the wavenumber on double logarithmic scales for two discharge types. The lines shown are power-law fits to the data assuming a k_{pol}^{m} dependency of the scattered power.

The exponents are m = –2.42/-3.01 for volumes 1/2 (Figure 9 left) and m = –2.79/-3.25 (Figure 9 right). The volumes were toroidally displaced so one wouldn't expect differences in the scaling. We conclude that the scaling is close to a k_{pol}^{-3} dependency. We would at this point like to mention that we have made other wavenumber scans in other discharge types where a 'rupture' in the scaling is observed at a characteristic wavenumber k_0. For wavenumbers smaller than k_0 we observe an approximate k_{pol}^{-3} scaling, for larger wavenumbers this changes to a k_{pol}^{-7} scaling [9].

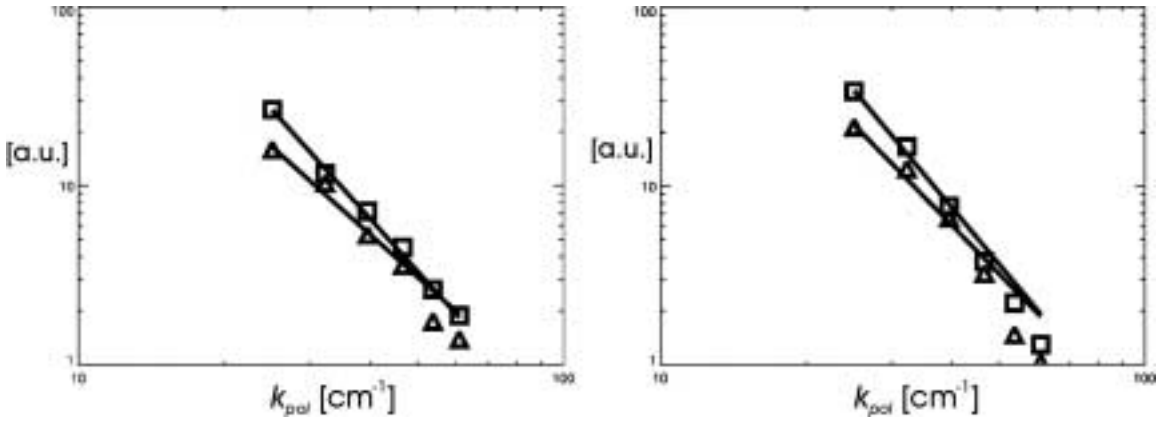

Figure 9. Steady-state frequency integrated power vs. wavenumber. Triangles are volume 1 points, squares volume 2. Left: Same discharge type (but here with Hydrogen) as in sections 3 and 4, right: Same discharge type but with $\iota_a = 0.361$ instead of 0.344.

2.2.1.6 The H-mode*

Our final subject in this chapter concerns a discharge with L-H* transitions, H* being the W7-AS ELM-free H-mode. As an overview we begin by showing power spectra vs. time and frequency ([-700,700] kHz) for volume 1 in Figure 10. The transitions are clearly seen as sudden drops in the scattered power. The final H*-mode lasts from 542 to 1000 ms where the discharge terminates. The increase in the fluctuations observed in the last H*-mode occurs because the density is continually ramped up.

To study the transition structure in more detail Figure 11 displays the scattered power from volume 1 in a 100 kHz band vs. time (black). The blue plot shows the H_α–signal to pinpoint the transitions. Both traces are normalised to [0,1] and the H_α–signal is displaced by minus one-half for clarity.

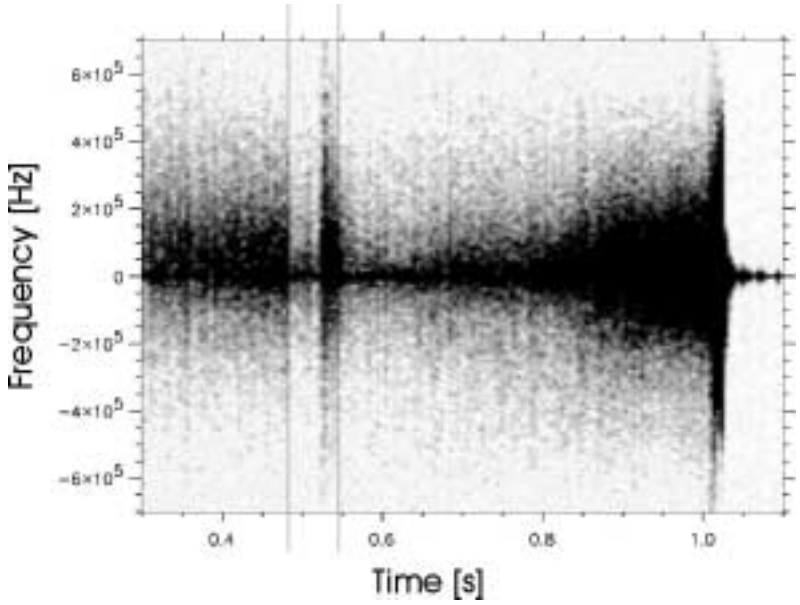

Figure 10. Power spectra for volume 1, k_{pol} = 31 cm^{-1}, shot 47061. The time resolution is 5 ms, frequency resolution 10 kHz. The two L-H* transitions are indicated by vertical lines. After the discharge ends at 1.0 s only the 40 MHz leak centered at 0 Hz remains.

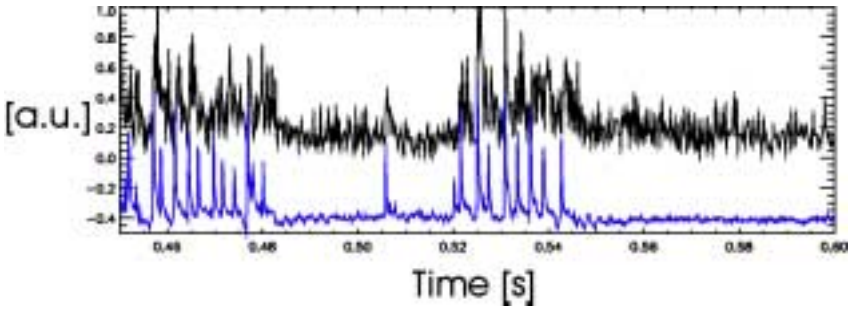

Figure 11. Close-up of the two L-H* transitions. Black trace is the scattered power in the [100,200] kHz band, time resolution 200 μs. The offset blue trace shows the H_α-signal as an L-H* transition marker. The 25 ms 'dither' back into L-mode consists of an ELM-bunch (9 ELMs).

To end this short H*-mode study we show how to normalise the scattered power by density. Theoretically, the scattered power is proportional to density squared, so we will normalise assuming this dependency. Figure 12 illustrates the procedure:

1. The scattered power is calculated (top)
2. The line density is retrieved from the W7-AS shotfile (center)
3. The power divided by squared density is calculated (bottom)

We conclude that the normalised fluctuations are decreasing in the L-mode phase leading up to the H*-mode; in the H*-mode the normalised fluctuations remain approximately constant.

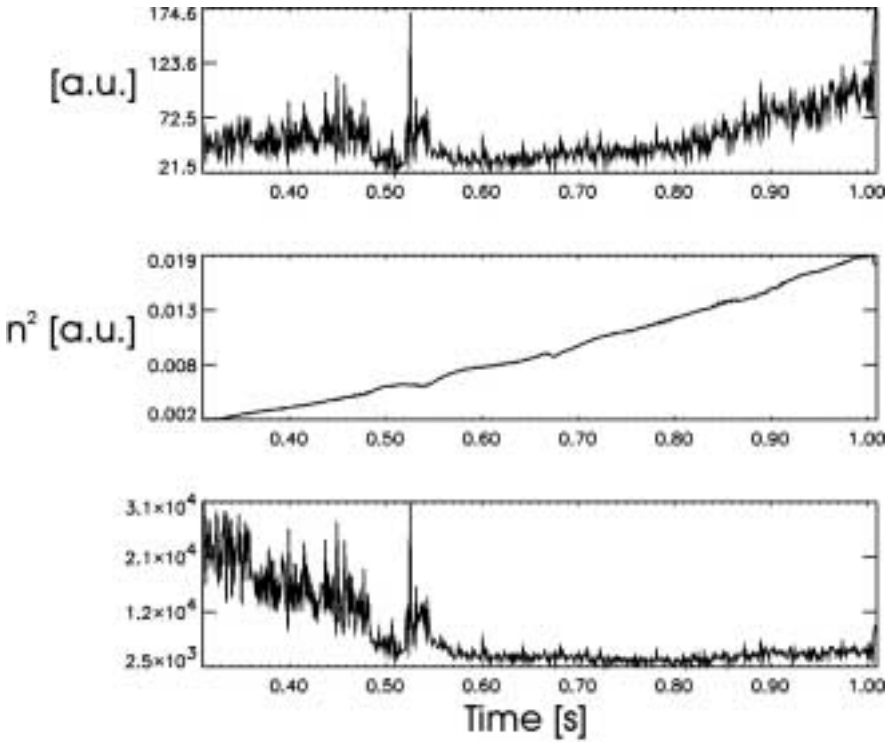

Figure 12. Scattered power between 100 and 200 kHz, time resolution 1 ms (top), squared density (center) and power divided by squared density (bottom).

2.2.1.7 Conclusions and outlook

1999 saw a breakthrough in measurements and analysis of the density fluctuations using the LOTUS diagnostic. This was due to intensive work both on data analysis programs (S. Zoletnik) and the optical system (M. Saffman). We routinely made measurements in the 1999 campaign from January to August and have accumulated a vast amount of data awaiting further analysis. About 80 dedicated shots exploring the current ramping experiments were made.

The main scientific results were:

- The scaling behaviour of density fluctuations was studied using wavenumber scans.
- The wide beam localisation was verified.
- A novel narrow beam localisation method was proposed and executed.
- A number of confinement regimes/transitions have been studied with emphasis on the current ramping experiments.

W7-AS will resume operations in summer 2000 when ten divertor modules have been installed. We are currently upgrading LOTUS (new optics, detectors etc.) and will continue measurements in the forthcoming campaign on W7-AS. At present, phase-separation techniques [10] and simulations are being constructed to assist in interpretation of the acquired data.

[1] Saffman M et al., Association EURATOM – Risø National Laboratory Annual Progress Report 1996.
[2] Truc A et al., Rev. Sci. Instrum. 63 (7) (1992) 3716-3724.
[3] Basse N P & Zoletnik S et al., 12th International Stellarator Conference (1999), Madison, Wisconsin, USA.
[4] Basse N P et al., 27th EPS (2000).
[5] Renner H, Plasma Phys. Control. Fusion Vol.31, No.10, 1579-1596 (1989).
[6] Baldzuhn J et al., Plasma Phys. Control. Fusion **40** (1998) 967-986.
[7] Brakel R et al., Plasma Phys. Control. Fusion **39** (1997) B273-B286.
[8] Basse N P et al., Department of Optics and Fluid Dynamics Progress Report 1999.
[9] Honoré C et al., 25th EPS ECA **22C** (1998) 647-650.
[10] Antar G et al., Plasma Phys. Control. Fusion **41** (1999) 733-746.

2.3 Nonlinear Dynamics of Fusion Plasmas

2.3.1 Stellarator geometry for a 3D code of drift Alfven turbulence

V. Naulin, S. B. Korsholm, P.K. Michelsen and J.J. Rasmussen

Plasmas relevant to thermonuclear fusion are characterised by a complicated structure of the confining magnetic field. While the poloidal component of the magnetic field in a tokamak is created via a toroidal current in the plasma, a so-called stellarator creates the magnetic field structure through complicated outer coils alone. This goes along with a loss in rotational symmetry. Magnetic field aligned coordinates thus vary in all three spatial dimensions. A numerical code reflecting this geometry therefore needs 3D information on the MHD equilibrium for which the stellarator has been optimised.

In collaboration with the IPP in Greifswald and CIEMAT in Madrid relevant stellarator geometries will be prepared for numerical drift Alfven simulations. In fusion plasmas the local change of the magnetic field due to the density fluctuations should be considered even for a small plasma beta. The existing TYR-code (See Risø-R-1100(EN) 1999, sec. 4.2.6) was therefore extended from an electrostatic three-field model to a five-field electromagnetic model where the parallel Alfven dynamics are considered. A verification of the code against the DALF codes of the IPP in Garching is planned.

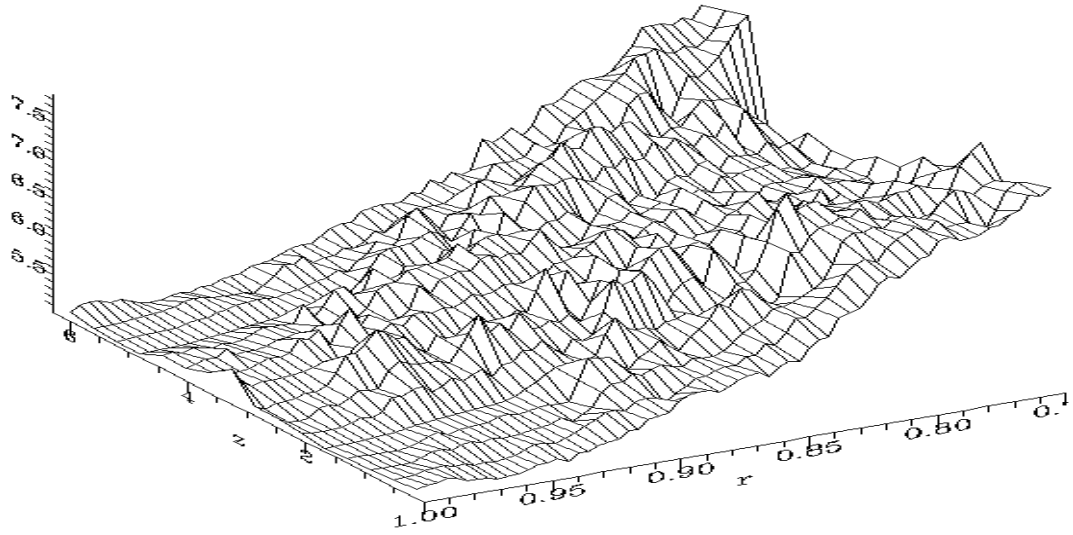

Figure 13: Density profile over radius and poloidal angle for a tokamak simulation. The unfavourable curvature at poloidal angle π is connected to a flattening of the density as fluctuation levels are higher there.

2.3.2 Three-dimensional flux driven drift wave simulations

S. B. Korsholm, V. Naulin, J. Juul Rasmussen and P. K. Michelsen

The understanding of turbulence and transport of plasma is crucial in the development of fusion energy. Several turbulence models have been developed and implemented at Risø with the aim of obtaining a better understanding of edge region plasma turbulence.

In the models it has most often been assumed that the plasma density gradient is constant, i.e. it is not perturbed by the turbulence. Another assumption that might be more realistic is to assume that the flux of density from the core of the plasma into the edge region is constant. Such flux driven systems are being implemented and preliminary results indicate that the turbulence is saturated due to a flattening of the gradients, see Figure 14. Furthermore, the saturation level of the turbulence is significantly lower than that for the gradient driven case.

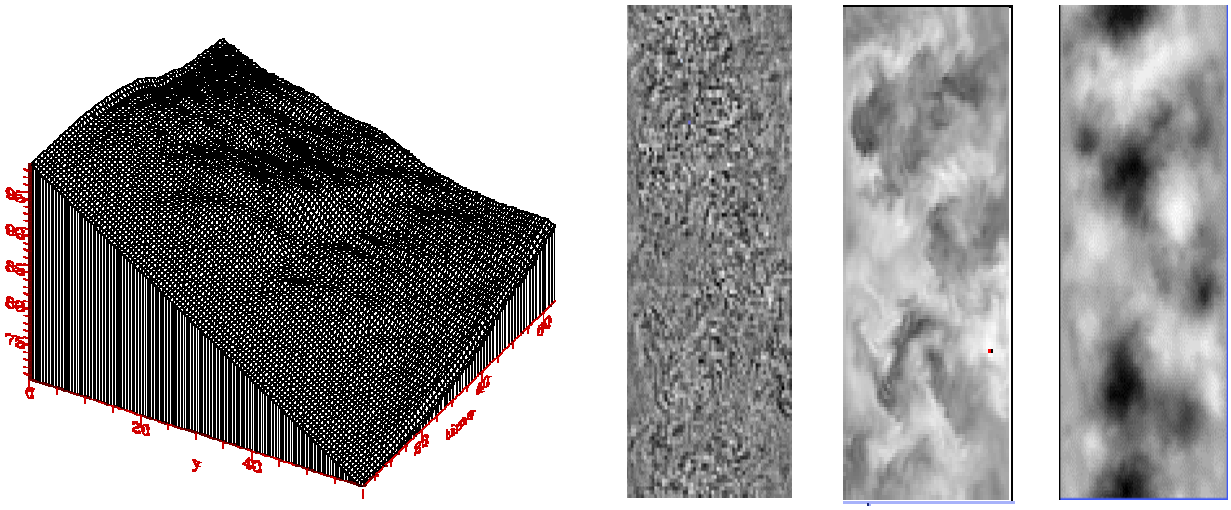

Figure 14. Evolution of background density over time (left) and turbulent vorticity, density and potential in a flux driven Hasegawa-Wakatani system..

2.3.3 Transport barriers in pressure driven flute mode turbulence

V. Naulin, J. Nycander (FOA, Stockholm, Sweden) and J. Juul Rasmussen

We investigate the evolution of turbulence and the associated formation of transport barriers in a model system for 2D electrostatic pressure driven flute modes. The fluctuations are flux driven and are generated via a Rayleigh-Taylor instability setting where the pressure gradient exceeds the magnetic field strength gradient. This pressure gradient is forced by a constant temperature difference between the two sidewalls of the computational domain. The temperature difference sustains a thermal flux.

Turbulent equipartition predicts the background profiles and gradients resulting from the homogenisation of the Lagrangian invariants due to the strong mixing by the turbulence. This is clearly revealed for large aspect ratios, $L_y/L_x > 2.2$, where x is in the direction of the gradients ("radial direction") and y is perpendicular to the gradients ("poloidal direction") (the confining magnetic field is in the z-direction). These profiles, which correspond to the marginally stable profiles, are flatter than the profiles that will result from classical viscous diffusion in the absence of the turbulence. For small aspect ratios, however, the numerical simulations show a strong tendency for the evolution of a poloidal shear flow that quenches the effective turbulent mixing and the transport changes from being anomalous, i.e. fluctuation driven, to being diffusive. Thus, a much steeper gradient evolves on a diffusive timescale. Subsequently, the resulting steep gradient is prone to the Rayleigh-Taylor instability again, and short burst-like destabilisations, which flatten out the profiles, occur locally. The transport associated with these burst-like events propagates down the background gradient and has properties of avalanche-like event. In Figure 15 we show the evolution of the heat flux for different aspect ratios.

The mechanisms for the shear flow generation and the influence of the shear flow on the turbulence are presently under investigation.

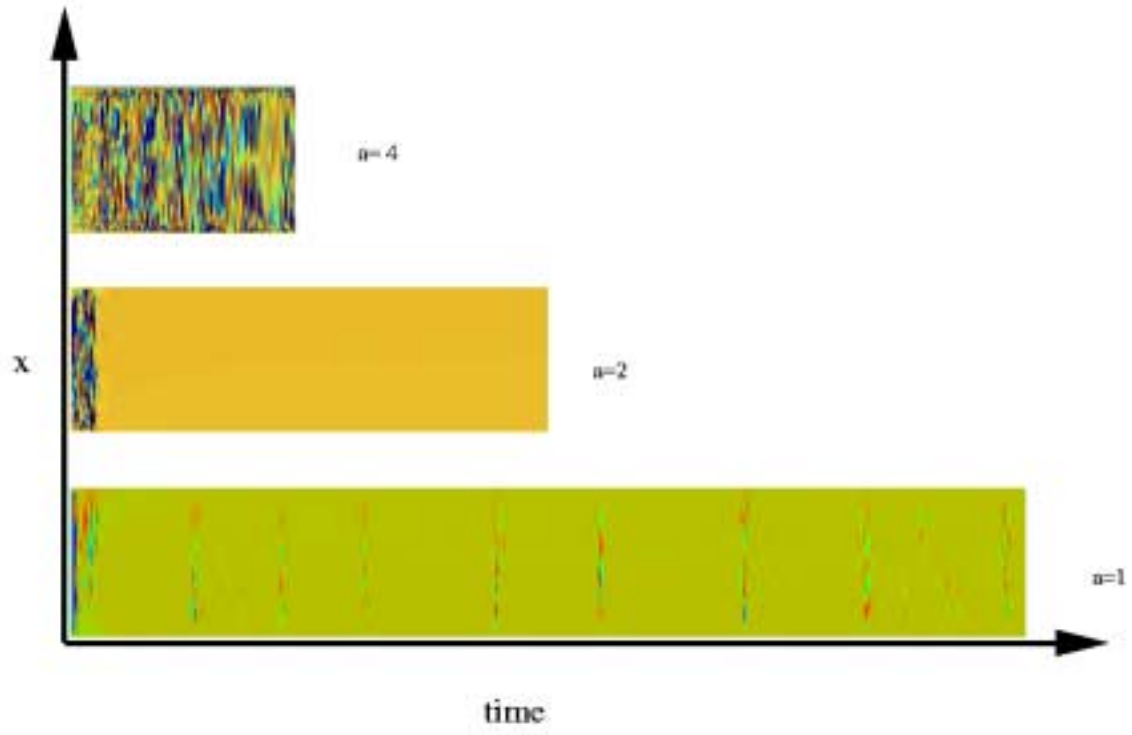

Figure 15. Time evolution of the poloidally averaged radial heat flux for three different values of the aspect ratio a = Ly/Lx. The system is heated from the left. For a = 1 the bursts occur at random intervals, with a characteristic time interval determined by the diffusive timescale.

2.3.4 Identification and tracking of vortices in turbulent flows

T. Jessen and P.K. Michelsen

Coherent vortices are a prominent feature of two-dimensional turbulence and have been observed in several plasma experiments. We have developed a new method for detecting and tracking vortices in turbulence simulations in order to quantify vortex properties and assess their importance. Two related algorithms have been developed: (1) identification of vortices from a frozen snapsnot (a "still") of the flow field, and (2) tracking of individual vortices from a sequence of stills.

In free 2D turbulence the vorticity field, i.e. the curl of the velocity field, tends to be concentrated in small regions of extreme values that form the vortex centres around which the fluid rotates. Often vorticity can be considered concentrated in points rather than being smeared out continuously, which results in a point vortex model. This model, however, becomes inappropriate when vortices of the same circulation approach each another. In this case the typical outcome is a vortex merger, an example of which is shown in Figure 16.

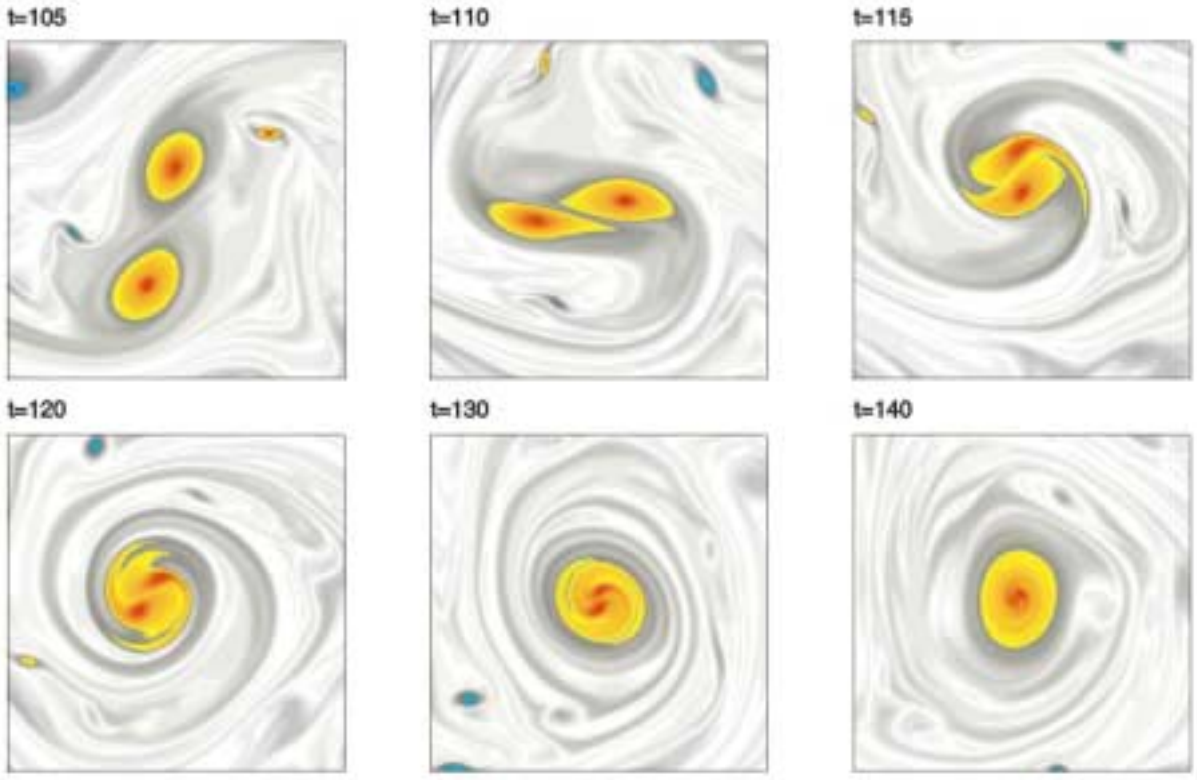

Figure 16. A vortex merger in a plasma turbulence simulation. A colour-coded vorticity (charge density) map is shown. Two positively charged vortices, of counterclockwise rotation, merge to form a single supervortex.

Vortex mergers tend to organise the flow into fewer, but larger, vortices and hence to transfer energy towards the large scales of motion. On the other hand, they also strain and filmentate fluid elements, thereby transferring enstrophy (vorticity squared) towards the smaller scales. Thus, they are intimately connected with the dual cascade of energy and enstrophy, which is characteristic of 2D turbulence.

Hitherto, quantitative analysis of coherent vortices has been restricted by the need for a human observer. Vortex behaviour has qualitatively been described on the basis of naked eye inspection of flow field plots. This is a time consuming and subjective procedure, and quantitative results are likely to be based on poor and biased statistics. In contrast, an automated procedure allows analysis of large data and yields representative statistics based on objective criteria.

A vortex identification algorithm has been developed. It is primarily based on the Weiss criterion, and essentially designates regions where rotation rate exceeds rate of strain as vortex candidates. An example is shown in Figure 17. The left-hand figure shows the instantaneous stream lines of a turbulent plasma flow. The right-hand figure shows the associated Weiss field, colour coded with vortex candidates coloured blue. Vortex candidates are marked with crosses and are seen to coincide with regions of closed streamlines.

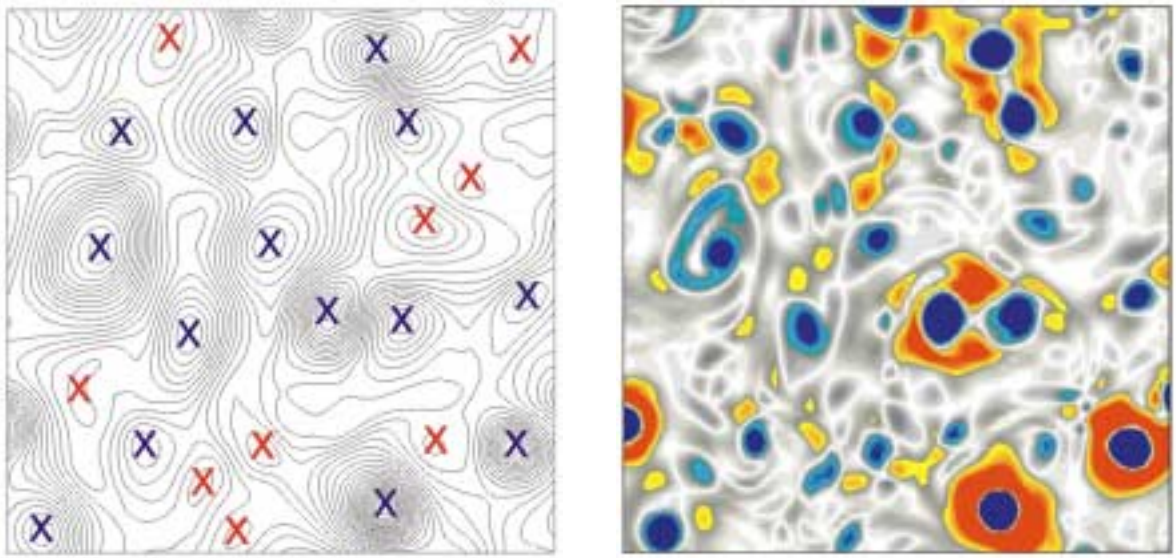

Figure 17. Left: Streamlines of a turbulent plasma flow. Vortical structures are indicated by crosses. Coherent structures are marked by blue crosses. Right: The associated Weiss field. Rotation dominated regions are blue, strain dominated regions are red.

A newly developed vortex tracking algorithm is capable of recording the fate of individual vortices and, hence, of calculating vortex lifetimes and diffusivities. This allows us to distinguish between incoherent temporary vortices, due to random fluctuations of the turbulent field, and persistent coherent vortices. In Figure 17 incoherent vortices have been marked with red crosses. Vortices existing for more than one full rotation period are said to be coherent and have been marked with blue crosses.

The automated vortex identification and tracking algorithms are now as a routine used to sample vortex statistics in turbulence simulations. Distributions of vortex size, mass, charge, lifetime, etc. are calculated and offer new insight into vortex dynamics.

2.3.5 Dispersion of ideal particles in developed 2D and 3D turbulence

V. Naulin, A.H. Nielsen and J. Juul Rasmussen

The dispersion properties of particles in inhomogeneous turbulence are still not well understood. Covering a variety of important areas from the diffusion of pollutants to the behaviour of heavy ions in fusion devices this area connects basic research with applications. In the past, idealised maps of the turbulence were used to elaborate on the diffusion of particles as turbulence simulations were not available for the long time series needed. Making use of Risø's 2D and 3D plasma turbulence codes, we are able to track a larger number of particles for rather long time compared with the fundamental frequencies of the considered system. Of special importance is the influence of coherent structures on the particle dispersion. Due to the appearance of travelling waves in the turbulence, the interaction between structures and waves is important as it changes the probability distribution of the velocity fluctuations. Then the variance of these fluctuations might not be well defined and sub- or super-diffusive (Levy Flights) behaviour is observed. The diffusion is anisotropic with respect to the background density gradient or the propagation direction of the travelling waves.[1]

1. Naulin, V., Nielsen, A.H. and Rasmussen, J.J. Phys. Plasmas **4** (1999), 4575 - 4585.

2.3.6 Reynolds stress and shear flow generation

S. B. Korsholm, V. Naulin, J. Juul Rasmussen and P. K. Michelsen and L. Garcia (Universidad Carlos III, Madrid, Spain)

One of the major challenges in the research towards a fusion power plant is the understanding and control of the plasma turbulence leading to anomalous transport of particles and energy. In various turbulence models it has been observed that shear flows suppress turbulence and, thereby, the associated transport. Poloidal flows might, indeed, be responsible for the so-called H-modes (High confinement modes), which are projected to be the standard for fusion reactors. These flows are generated and affected by several effects and the full mechanisms are not yet fully understood. In this numerical work we investigate the relation between the so-called Reynolds stress[1] and the poloidal flow generation.

The model used in the numerical investigations is the three-dimensional drift wave Hasegawa-Wakatani model.[2] The simulations are performed in a slab geometry periodic in y and z (corresponding to the poloidal and the toroidal directions, respectively) while we use non-permeable walls in the radial direction, i.e. Dirichlet boundaries in x, ϕ (x=0)= ϕ(x=L_x)=0 and n(x=0)=n(x=L_x)=0, where ϕ is the electrostatic potential fluctuations, n is the density fluctuations and L_x is the domain length. The simulations are performed using pseudo-spectral methods in the periodic directions and finite difference methods in the bounded direction.

The Reynolds stress is a measure of the anisotropy of the turbulent velocity fluctuations that produce a stress on the mean flow. This may cause acceleration of the flow in the plasma, which could e.g. be a poloidal flow (y-direction).

To determine the Reynolds stress defined as:

$$\mathrm{Re}_\phi = -\langle v_x v_y \rangle = \left\langle \frac{\partial \phi}{\partial y} \frac{\partial \phi}{\partial x} \right\rangle,$$

one needs the value of the fluctuations in the potential. Since accurate measurements of the potential perturbations are quite difficult, especially in large plasma devices, a pseudo-Reynolds stress based on much easier obtainable density measurements has been proposed. The pseudo-Reynolds stress is defined as:

$$\mathrm{Re}_n = \left\langle \frac{\partial n}{\partial y} \frac{\partial n}{\partial x} \right\rangle.$$

We find that the Reynolds stress Re_ϕ and the pseudo-Reynolds stress Re_n are strongly correlated with a correlation of 0.8. The reason for the strong correlation between Re_n and Re_ϕ is that the density and the potential fluctuations are strongly correlated for drift waves.

.

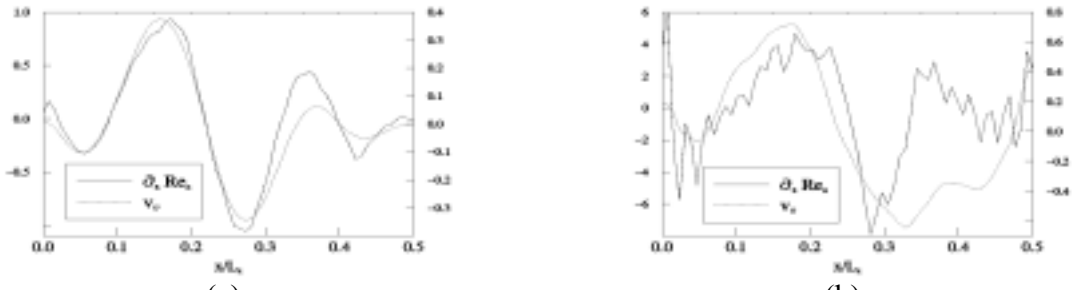

(a) (b)

Figure 18. The poloidal flow compared with the flow predicted by the drift wave pseudo-Reynolds stress at two instants in time a) t=75 and b) t=100.

The conclusion of this is that the pseudo-Reynolds stress gives a good estimate of the real Reynolds stress and it may thus be possible to predict flow generation by measuring density fluctuations. In Figure 18 we compare the poloidal flow with the flow predicted by the pseudo-Reynolds stress. The observed behaviour may, however, be specific to this particular turbulence model and more models have to be investigated

1. D. J. Triton, *Physical Fluid Dynamics*, Clarendon Press, Oxford, 2nd ed., 1988, Chapter 19.
2. A. Hasegawa and M. Wakatani, Phys. Rev. Lett. **50** (1983) 682-686.

2.3.7 Comparison of simulations with simple plasma experiments

V. Naulin, D. Block, F. Greiner*, U. Grulke*, S. Niedner*, A. Piel* and U. Stroth**
*(*Christian-Albrechts-Universität, Kiel, Germany)*

Small-sized plasma experiments with a simple geometry are an ideal playground to test various hypotheses concerning, e.g., statistics of plasma turbulence, plasma transport and the appearance of coherent structures in these nearly 2D systems. Well-developed diagnostics and good control of the experiments make it possible to verify numerical codes with these experiments. Their relatively low plasma temperatures put the relevant spatial sizes in a range where today's numerical resolution is sufficient to simulate the whole plasma cross section. At Kiel University probe measurements of the linear experiment KIWI and the simple magnetised torus TEDDI will be compared with results from Risø's 2D and 3D codes. Information about coherent structures, turbulent transport and statistical properties of the plasma turbulence will be obtained. Initial simulations show a reproduction of the weak turbulence regime observed in the KIWI discharge. Unique and essential properties of theory and modelling will be matched with experimental results. Advanced methods for time series analysis will be used as well as visualisation of the turbulent fields. As a second step we plan to perform a comparison of the numerical results with measurements from the geometrical much more complex TJ-K. A goal will be to isolate the most important and persistent ingredients to the turbulence as the turbulence often shares similar behaviour between experiments of different sizes and geometries.

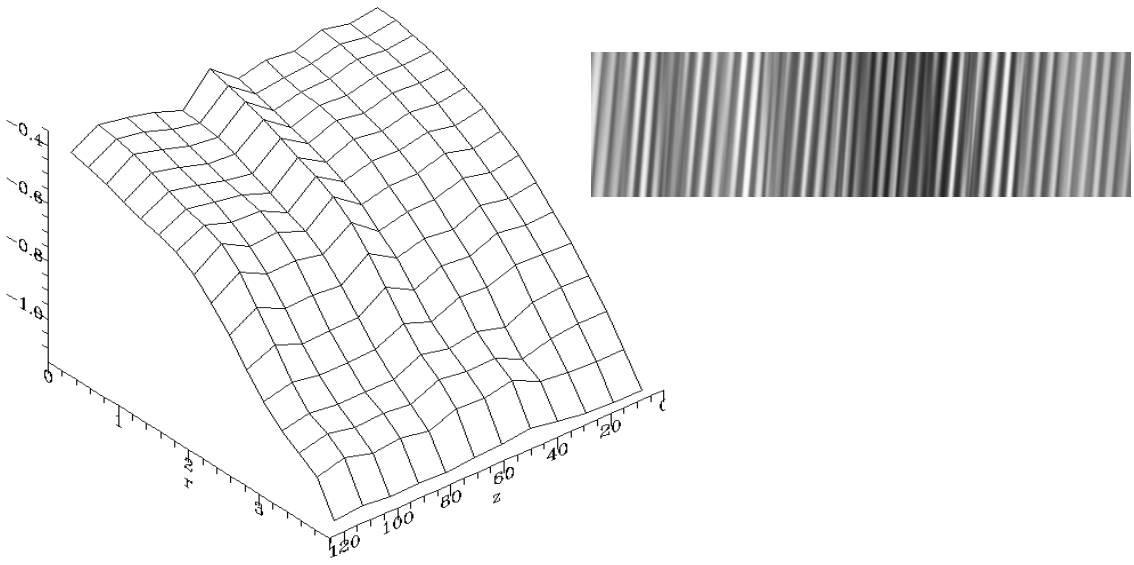

Figure 19. Logarithm of density over radius and azimuthal position for a simulation of the KIWI discharge (left). Poloidal potential fluctuations over 1000 time units. A mode m=2 is observed (right).

2.3.8 Homogenisation of potential vorticity and formation of poloidal flows

J. van de Konijnenberg, V. Naulin, J. Juul Rasmussen and B. Stenum

We investigate the formation of poloidal flows via homogenisation of Lagrangian invariants in a model for a cylindrical plasma. With a background density peaked in the center of a disk we consider fluctuations of the drift wave type with a Boltzmann relation connecting potential and density fluctuations. As an internal instablilty is absent in this system we drive density perturbations at an outer layer. With a constant density gradient $\beta = -dn/dr$ we have the so-called potential vorticity $PV = \omega - \varphi/\rho^2 + \beta r$ as a Lagrangian invariant, with φ being the potential fluctuations, ω the vorticity and ρ the ion Larmor radius at electron temperature. Depending on these parameters and the viscosity numerical simulations of the plasma reveal the appearance of banded poloidal flows, each of which corresponds to a local equidistribution of PV. An example is shown in Figure 20. The shear created by theses flows act as transport barriers and are thus of outmost importance in the understanding of plasma confinement. A more detailed analysis on the parameter dependence of these flows is currently undertaken.

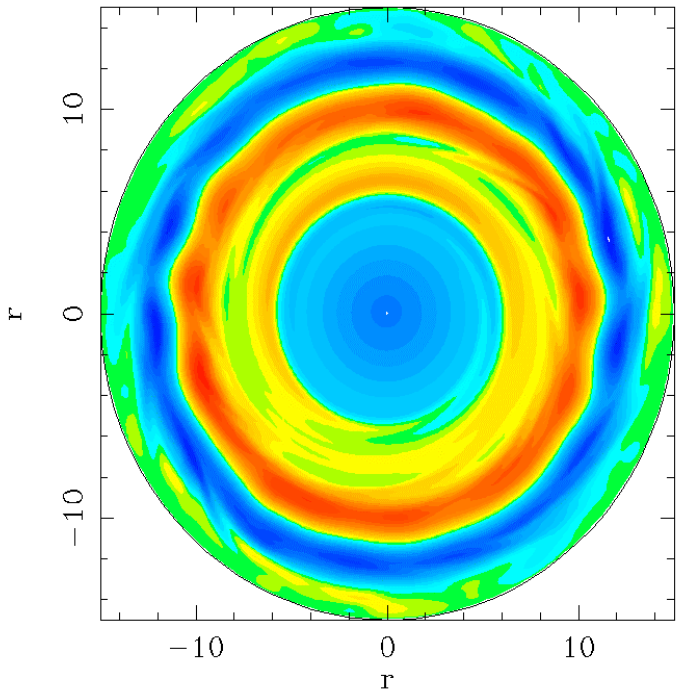

Figure 20. Vorticity in a simulation of drift-wave turbulence in a section of a cylindrical plasma with driving at two azimuthal position at r=9.

Recalling the analogy between drift-wave dynamics and Rossby wave dynamics on the β-plane we performed the corresponding laboratory experiment in a rotating fluid with sloping bottom to investigate experimentally the formation of large-scale flows by mixing and homogenisation of potential vorticity. These experimental investigations are not supported by Euratom. We use a rotating tank with radially symmetric bottom topography and a rigid lid. The bottom has a constant slope in the radial direction; the slope may be either negative (the shallowest part is at the centre) or positive (the deepest part is at the centre). For this system the potential vorticity is given by $PV = \omega + \beta r$. Here ω is the relative vorticity and β is proportional to the slope of the bottom. In the fluid case he turbulence is driven by locally

injecting and rejecting fluid periodically near the outer boundary of the tank at two azimuthal positions opposite to each other.

Results are that for $\beta < 0$ an effective mixing that homogenises PV leads to replacing the high PV near the centre with low PV from the outside: An anticyclonic vortex appears over the centre. For $\beta > 0$, e.g., the plasma case, a cyclonic vortex appears in the center. In both cases a flow opposite to the central one is found in the outer region of the tank, with a sheared region in between.

2.4 Special Projects

2.4.1 Pellet injectors

P.K. Michelsen and B. Sass

Technical advice of pellet injectors has been given through 1999. A visit of Mr. Sass to Frascati in March with the purpose to install a two stage gas gun instead of one of the eight single stage guns on the Risø produced injector was very successful. Ongoing discussions during 1999 with Culham Science Centre about installation of the eight-shot pellet injector from RTP on MAST have resulted in two visits to Culham during the beginning of 2000. During the second visit the pellet injectors was tested successfully by shooting deuterium pellets towards a dummy target. It has now been decided that the injector unit will be send to Risø where the barrels will be changed in order to get the possibility for larger pellets.

2.4.2 Laser anemometry for wind turbines

L. Lading, R. Skov Hansen and S. Frandsen (Wind Energy and Atmospheric Physics Department)

The work on plasma diagnostics based on collective scattering of laser light has given the Association a competence within light scattering, CO_2 laser technology, and light beating. This knowledge is being applied in a very different context, namely long range wind velocity measurements for power curve measurements and control of wind turbines. The aim is a very compact and robust system that is mounted on the nacelle of a turbine and measures the instantaneous wind velocity several hundred meters upstream.

Two systems for detecting the Doppler shift are under consideration for the wind turbine anemometer: The heterodyne principle, where the collected light interferes with a local oscillator withdrawn from the same laser as giving the focused beam. The beat frequency between the two signals is measured with a photo detector and is equal to the Doppler shift introduced on the back-scattered light. In the autodyne principle, the back-scattered light is again collected through the same telescope used for focusing the output beam. The back-scattered light enters the same laser delivering the focused beam, which gives rise to a small perturbation of the laser power. The Doppler shift is measured from the fluctuations of the laser power. The telescope for focusing the output beam and collecting the back-scattered light is planned to be consisting of a set of off axis parabolic mirrors. In order to establish the local oscillator and the mixing, the heterodyne detection system requires a number of optical components apart from a detector, the laser, and the telescope, whereas the autodyne system only consists of the laser, the telescope, and the detector. On the other hand, the autodyne set-up introduces more constraints on the laser, which are presently under consideration. During

1999 both the heterodyne and the autodyne system have been demonstrated in a scaled set-up using a 2W CO_2 laser and a refractive telescope focusing the output beam 10 meters away. A proof-of-principle was hereby established. Digital signal processing of the measured Doppler signal will be integrated in the final anemometer.

The project is not supported by Euratom, but is partly funded through the EU Joule programme. The partners in the project incorporate the world largest manufacturer of wind turbines, *NEG-Micom* (Denmark), a major manufacturer of CO_2 lasers, *Ferranti Photonics Limited* (United Kingdom), and a small-and-medium-size-enterprise WEA-Engineering (Denmark).

2.4.3 Lectures in Plasma Physics

P.K. Michelsen

A course in fundamental Fusion Plasma Physics is given regularly every autumn semester. The course in taught in 27 double lectures either in Danish or English if these are English-speaking students. The book *Introduction to Plasma Physics* by R.J. Goldston and P.H. Rutherford is used for most of the course. The students finish the study by an oral examination. A special course in Fusion Reactor Physics is given during the spring semester 2000 with a three days study tour to Culham and JET included.

2.5 Participants in Fusion Plasma Physics

2.5.1 Scientific staff

Glückstad, Jesper (part time)
Jensen, V.O. (until 31 January)
Lading, Lars (until 31 September) (part time)
Larsen, Henning (part time)
Lynov, Jens-Peter
Michelsen, Poul K.
Naulin, Volker (from 1 April)
Nielsen, Anders H.
Rasmussen, Jens Juul
Saffman, Mark (until 30 September)

2.5.2 Post docs

Dinesen, Palle
Naulin, Volker (until 31 March)

2.5.3 PhD students

Basse, Nils
Jessen, Thomas (until 30 September)
Korsholm, Søren Bang

2.5.4 Technical staff

Astradsson, Lone
Jessen, Martin
Sass, Bjarne
Thorsen, Jess

2.5.5 Guest scientists

Hesthaven, Jan S., Brown University, Rhode Island, USA
Karpman, Vladimir, Racah Institute of Physics, Hebrew University, Jerusalem, Israel
Saffman, Mark, University of Wisconsin-Madison, USA
Wyller, John, Agricultural University of Norway, Norway

2.5.6 Short-term visitors

Antar, Ghassan, Association Euratom-CEA, DRFC, CEA/Cadarache, France
Bergé, Luc, Commissariat à l'Energie Atomique, Centre d'Etudes de Limeil-Valenton, France
Germaschweski, Kai, University of Düsseldorf, Germany
Gonzalo, Luis Garcia, University Carlos III, Madrid, Spain
Grauer, Rainer, University of Düsseldorf, Germany
Krane, Bård, University of Oslo, Norway (10-12/2)
Mezentsev, Vladimir K., Aston University, United Kingdom
Milligen, Boudewijn van, Ciemat, Madrid, Spain
Paulsen, Jim-Viktor, University of Tromsø, Norway
Pasmanter, Ruben, Royal Dutch Meteorological Institute, Holland
Schäfer, Tobias, University of Düsseldorf, Germany

2.6 Publications

2.6.1 International publications

Chakrabarti, N., Steady state drift vortices in plasmas with shear flow in equilibrium. Phys. Plasmas (1999) v. 6 p. 417-419.

Chakrabarti, N.; Juul Rasmussen, J., Shear flow effect on ion temperature gradient vortices in plasmas with sheared magnetic field. Phys. Plasmas (1999) v. 6 p. 3047-3056.

Korsholm, S.B.; Michelsen, P.K.; Naulin, V., Resistive drift wave turbulence in a three-dimensional geometry. Phys. Plasmas (1999) v. 6 p. 2401-2408.

Korsholm, S.B.; Michelsen, P.K.; Pécseli, H.L., Nonlinear dynamics of resistive electrostatic drift waves. Phys. Scr. (1999) v. T82 p. 12-16.

Naulin, V.; Juul Rasmussen, J., Vortex dynamics in inhomogeneous plasmas. Phys. Scr. (1999) v. T82 p. 28-31.

Naulin, V.; Nielsen, A.H.; Juul Rasmussen, J., Dispersion of ideal particles in a two-dimensional model of electrostatic turbulence. Phys. Plasmas (1999) v. 6 p. 4575-4585.

2.6.2 Danish publications

Jensen, V.O., Fusionsenergi - hvor langt er vi nået?. Nat. Verden (1999) v. 82 (no.4) p. 14-25.

Lynov, J.P.; Singh, B.N (eds.), Association Euratom - Risø National Laboratory annual progress report for 1998. Risø-R-1136(EN) (1999) 46 p.

2.6.3 Conference lectures

Jessen, T.; Michelsen, P.K., Spectral time series analysis of plasma turbulence. In: Contributed papers. 26. European Physical Society conference on controlled fusion and plasma physics, Maastricht (NL), 14-18 Jun 1999. Schweer, B.; Oost, G. Van; Vietzke, E. (eds.), (European Physical Society, Mulhouse, 1999) (Europhysics conference abstracts, vol. 23J) p. 557-560.

Korsholm, S.B.; Michelsen, P.K., Density and temperature gradient driven drift waves. In: Contributed papers. 26. European Physical Society conference on controlled fusion and plasma physics, Maastricht (NL), 14-18 Jun 1999. Schweer, B.; Oost, G. Van; Vietzke, E. (eds.), (European Physical Society, Mulhouse, 1999) (Europhysics conference abstracts, vol. 23J) p. 59-552.

Michelsen, P.K.; Korsholm, S.B.; Pécseli, H.L., Three dimensional studies of a modified Hasegawa-Wakatani model. In: Contributed papers. 26. European Physical Society conference on controlled fusion and plasma physics, Maastricht (NL), 14-18 Jun 1999. Schweer, B.; Oost, G. Van; Vietzke, E. (eds.), (European Physical Society, Mulhouse, 1999) (Europhysics conference abstracts, vol. 23J) p. 553-556.

Naulin, V., Structure detection in driven drift wave turbulence. In: Simulation and identification of organized structures in flows. IUTAM symposium, Lyngby (DK), 25-29 May 1997. Sørensen, J.N.; Hopfinger, E.J.; Aubry, N. (eds.), (Kluwer Academic Publishers, Dordrecht, 1999) (Fluid mechanics and its applications, v. 52) p. 409-418.

Naulin, V.; Juul Rasmussen, J.; Nycander, J., Transport barriers in a model for turbulent equipartition. In: Contributed papers. 26. European Physical Society conference on controlled fusion and plasma physics, Maastricht (NL), 14-18 Jun 1999. Schweer, B.; Oost, G. Van; Vietzke, E. (eds.), (European Physical Society, Mulhouse, 1999) (Europhysics conference abstracts, vol. 23J) p. 545-548.

Naulin, V.; Korsholm, S.; Michelsen, P.K., Three-dimensional simulations of drift-wave turbulence. In: Theory of fusion plasmas. International School of Plasma Physics "Piero Caldirola": Joint Varenna-Lausanne international workshop (ISSP 18), Varenna (IT), 31 Aug - 4 Sep 1998. Connor, J.W.; Sindoni, E.; Vaclavik, J. (eds.), (Editrice Compositori, Bologna, 1999) p. 505-510.

2.6.4 Unpublished Danish lectures

Juul Rasmussen, J., Collaps and coherent structures in nonlinear optical media. Ph.D. course on nonlinear waves, coherent structures and stochastic dynamics, Technical University of Denmark (4 lectures), Lyngby (DK), 11-12 Nov 1999. Unpublished.

Korsholm, S.B.; Lynov, J.P.; Michelsen, P.K., Fusion energy research. In: Programme. Abstracts. List of participants. Annual meeting of the Danish Physical Society, Nyborg (DK), 3-4 Jun 1999. (HCØ Tryk, København, 1999) p. AF18P.

Michelsen, P.K., Fusionsenergi - er det en mulighed?. Foredrag på Danmarks Tekniske Universitet, Lyngby (DK), 25 Oct 1999. Unpublished.

Michelsen, P.K., Fusionsenergi - er det en mulighed?. Foredrag på Danmarks Tekniske Universitet, Lyngby (DK), 7 Oct 1999. Unpublished.

Michelsen, P.K., Forelæsninger i plasmafysik (54 forelæsninger) på Danmarks Tekniske Universitet, Lyngby (DK), Sep. – Dec. 1999. Unpublished.

2.6.5 Unpublished international lectures

Jensen, V.O., The physics behind diffusion caused by collision between like particles. 34. Nordic plasma and gas discharge symposium, Geilo (NO), 24-27 Jan 1999. Unpublished.

Juul Rasmussen, J., Statistical properties of cross-field plasma transport: Vortices, avalanches and self-organization. Fluctuations in fusion and non-fusion plasmas. TTF Turbulence Working Group, Padova (IT), 3-4 Mar 1999. Unpublished.

Juul Rasmussen, J., Vortex dynamics and particle transport in electrostatic turbulence of magnetized plasmas. 1999 plasma Easter meeting on nonlinear phenomena in fluids and plasmas, Turin (IT), 7-9 Apr 1999. Unpublished.

Juul Rasmussen, J., Turbulent equipartition in plasma and fluid. International workshop on solitons, collapses and turbulence: Achievements, developments and perspectives, Chernogolovka (RU), 3-10 Aug 1999. Unpublished.

Juul Rasmussen, J., Introduction to the Study Centre: Coherent structures. 1999 TAO Study Centre, Palma de Mallorca (ES), 6 Sep - 1 Oct 1999. Unpublished.

Juul Rasmussen, J.; Naulin, V., Cross-field plasma transport, avalanches, self-organized criticality and vortex dynamics. 34. Nordic plasma and gas discharge symposium, Geilo (NO), 24-27 Jan 1999. Unpublished.

Juul Rasmussen, J.; Nycander, J.; Naulin, V., Transport barriers in a model for turbulent equipartition. In: Programme and abstracts. 8. European fusion theory conference, Como (IT), 27-29 Oct 1999. (Istituto di Fisica del Plasma "Piero Caldirola", Milano, 1999) OW 7.

Korsholm, S.B.; Michelsen, P.K.; Naulin, V.; Juul Rasmussen, J., Poloidal flows and transport in non-periodic 3D simulations of the Hasegawa-Wakatani model. IAEA Technical Committee meeting on first principle-based transport theory, Monestery Seeon (DE), 21-23 Jun 1999. Unpublished. Abstract available.

Korsholm, S.B.; Michelsen, P.K.; Naulin, V., Three dimensional drift wave simulations. In: Programme and abstracts. 8. European fusion theory conference, Como (IT), 27-29 Oct 1999. (Istituto di Fisica del Plasma "Piero Caldirola", Milano, 1999) PT 12.

Korsholm, S.B.; Naulin, V., Plasma transport, zonal flows and Reynolds stress in 2 and 3D models of drift wave turbulence. Nonlinear science festival 2, Risø (DK), 1-4 Dec 1999. Unpublished.

Naulin, V., Vortex dynamics and Reynolds stress in dift-wave simulations. Fluctuations in fusion and non-fusion plasmas. TTF Turbulence Working Group, Padova (IT), 3-4 Mar 1999. Unpublished.

Naulin, V., Role of polarization drift in drift wave simulations. TTF turbulence workshop, Madrid (ES), 24-26 Mar 1999. Unpublished.

Naulin, V., Cross field plasma transport and poloidal flows. IAEA Technical Committee meeting on first principle-based transport theory, Monastery Seeon (DE), 21-23 Jun 1999. Unpublished.

Naulin, V., Closing the gap between numerics and experiment. 28. Steering Committee meeting, Risø (DK), 26. Apr 1999. Unpublished.

Naulin, V., Homogenization of potential vorticity. 1999 TAO Study Centre, Palma de Mallorca (ES), 6 Sep - 1 Oct 1999. Unpublished.

Naulin, V.; Juul Rasmussen, J.; Nycander, J., Zonal flow and transport barriers in turbulent equipartition. 34. Nordic plasma and gas discharge symposium, Geilo (NO), 24-27 Jan 1999. Unpublished.

Naulin, V.; Juul Rasmussen, J.; Nycander, J., Transport barriers in a model for turbulent equipartition. Seminar at Düsseldorf University, Düsseldorf (DE), Dec 1999. Unpublished.

Naulin, V.; Korsholm, S.B.; Michelsen, P.K.; Juul Rasmussen, J., Plasma transport, zonal flows, and Reynolds stress in 2 and 3D models of drift wave turbulence. In: Programme and abstracts. 8. European fusion theory conference, Como (IT), 27-29 Oct 1999. (Istituto di Fisica del Plasma "Piero Caldirola", Milano, 1999) PT 14.

Naulin, V.; Nielsen, A.H.; Juul Rasmussen, J., Transport und Disposition idealer Teilchen in 2-dimensionaler Turbulenz. Kolloquium at Kiel University, Kiel (DE), Dec 1999. Unpublished.

3. Fusion Technology

3.1 Introduction

The work reported in this section has been carried out in the Materials Research Department. The overall objective of the research activities in this area is to determine the impact of neutron irradiation on physical and mechanical properties of metals and alloys, so that appropriate materials can be chosen for their application in an irradiation environment (e.g. in a fusion reactor). Various experimental techniques are employed to study different aspects of the microstructural evolution during irradiation and the resulting consequences on the post-irradiation physical and mechanical properties of metals and alloys. Computer simulations are carried out to understand the evolution of surviving defects and their clusters in collision cascades. The kinetics of defect accumulation during irradiation and the influence of irradiation-induced defects and their clusters on the deformation behaviour of irradiated metals and alloys are studied theoretically. In the following, the main results of these activities are highlighted.

3.2 Next Step Technology

3.2.1 Cyclic deformation behaviour of copper alloys in unirradiated and irradiated conditions

B.N. Singh, J.F. Stubbins (*University of Illinois, Urbana-Champaign, USA) and P. Toft*

Currently, two copper alloys, one dispersion strengthened Glid Cop CuAl-25 and one precipitation hardened CuCrZr, are under evaluation for their use in the first wall and divertor components of ITER. These components will be exposed to an intense flux of 14 MeV neutrons and will experience thermo-mechanical cyclic loading as a result of the cyclic nature of plasma burn operations of the system. It is therefore of a crucial interest to determine and understand the cyclic deformation behaviour of these alloys operating in an irradiation environment. In the previous report, the fatigue lives of both unirradiated and irradiated CuAl-25 and CuCrZr alloys, irradiated and tested at 250 and 350^{o}C, were presented. These results demonstrated that at these temperatures irradiation causes a marked decrease in the lifetime of both alloys, most pronounced in the case of the CuAl-25 alloy at 350^{o}C.

In order to understand the nature of the cyclic deformation and thus the reason for fatigue failure in these alloys, the experimental results were further analysed in terms of elastic and plastic portions of the fatigue life response. This perspective is useful in understanding certain features of the fatigue life response for the various material, irradiation and test conditions. In order to provide a physical basis for the conclusions emerging from these analyses, the post-fatigue microstructures were investigated using transmission electron microscopy (TEM) and the fracture surfaces were examined using scanning electron microscope (SEM).

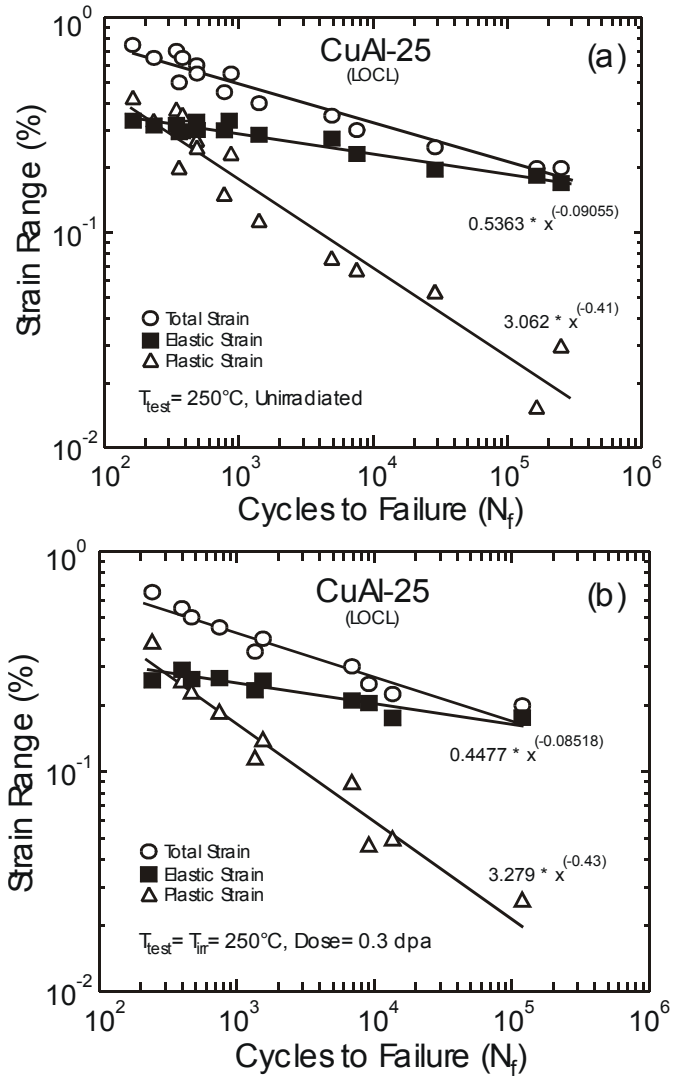

Figure 21. Cycles to failure (N_f) as a function of elastic, plastic and total strain range for CuAl-25 (LOCL) tested at 250°C (a) in the unrradiated and (b) irradiated condition.

An overall picture emerging from the present results and the results published earlier on the microstructural and the mechanical performance of the dispersion strengthened Glid Cop alloys (e.g. CuAl-25 (LOCL), CuAl-25 (IG0) and CuAl-60) is that the high density of alumina particles is very effective in restricting dislocation generation and migration. Consequently, these alloys were unable to deform plastically to any large extent both in unirradiated and irradiated conditions (Figure 21). However, since the spatial distribution of these particles is very heterogeneous (a fraction of grains contain no particles at all!) and these alloys contain very large volume fractions of grains and subgrain boundaries, it is inevitable that at high stresses, the weak components of the microstructure would begin to deform plastically but only in a localized form. It is thus possible that at high stresses cracks may nucleate at these weak boundaries and may propagate along them. All other microstructural evidence and fractography results are consistent with this picture and help rationalize not only the fatigue performance, but also tensile, fracture toughness, crack nucleation and growth behaviour of these alloys. This evaluation, of course, is not very encouraging from the point of view of

practical applications of this material in structural components. Unfortunately, it is not obvious as to how the basic microstructure of these alloys could be transformed from a heterogeneous to a homogeneous one so that these alloys can deform plastically in a homogeneous fashion. The answer may lie in the improvement of the manufacturing process.

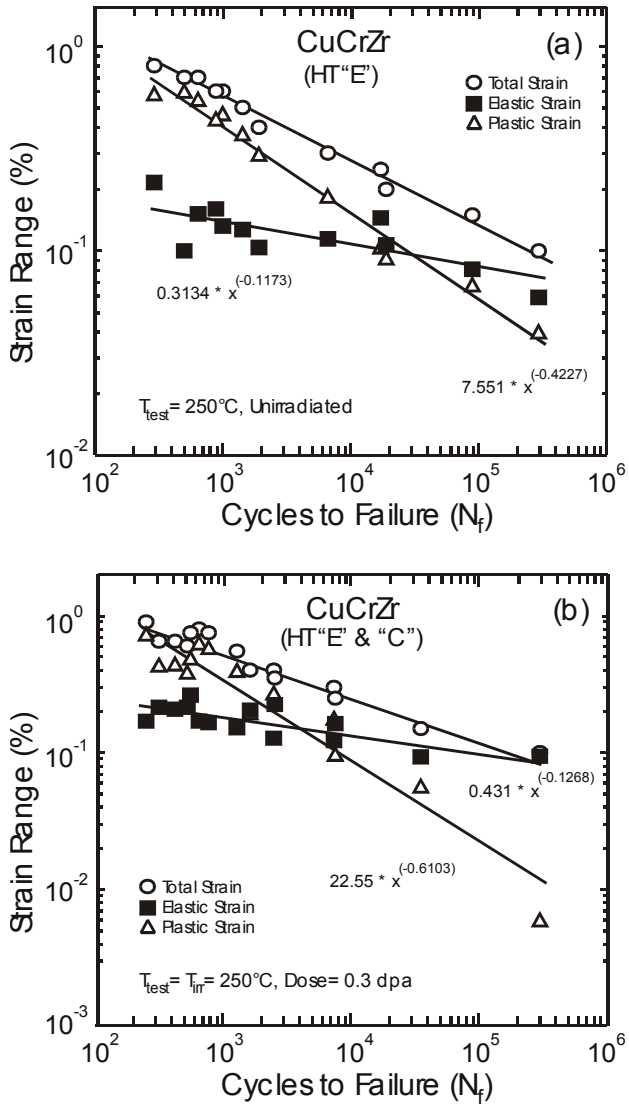

Figure 22. Cycles to failure (N_f) as a function of elastic, plastic and total strain range for the CuCrZr-alloy tested at 250°C (a) in the unrradiated and (b) irradiated condition.

The CuCrZr alloy presents a different set of problems. This work and earlier work indicate that it has certain appealing properties from a structural standpoint, particularly its residual plasticity that accounts for its superior fatigue performance at high strain ranges (see Figure 22). This performance is predicated on the ability to obtain an optimal microstructure by heat treatment. As with other precipitation hardened alloys, the size and distribution of the final precipitate population is very sensitive to proper heat treatments. Like in the case of dispersion strengthened alloys, heterogeneous microstructures are bound to behave poorly. A further concern for the CuCrZr alloys is their sensitivity to irradiation. It is clear in the foregoing that radiation has a visible effect on the mechanical performance. This is evident

from the microstructures in the 50°C irradiation case, and the irradiation hardening effect that is seen in the elastic strain range response and in the accompanying microstructure, particularly evident at 350°C. The challenge in the case of CuCrZr seems to be both with the potential difficulty of producing optimal microstructures in real components, and with the stability of the microstructure under both irradiation and deformation conditions.

3.2.2 Effects of HIP thermal cycles and neutron irradiation on tensile properties of copper/stainless steel joints

B.N. Singh and P. Toft

The present design of the ITER Plasma Facing Components consists of a copper alloy heat sink layer between plasma facing materials and stainless steel, the structural material. The main option for manufacturing these components is the Hot Isostatic Pressing (HIP) method. It is expected that more than one HIP thermal cycle may be necessary for manufacturing the final components. At present very little is known about the effects of successive HIP thermal cycles on the properties of the base alloys and the joints particularly in the hostile environment of energetic neutrons. The present study was undertaken to investigate some of these effects. In the following results are reported on the effects of HIP thermal cycles and neutron irradiation on tensile properties of HIP joints between CuAl-25 (IGO) and CuCrZr (Outokumpu OY) alloys and 316 (LN) austenitic stainless steel.

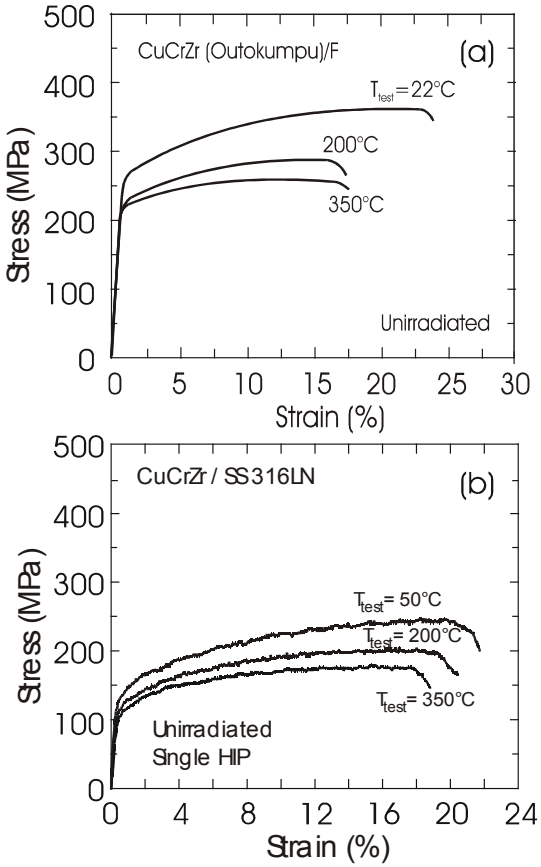

Figure 23. Stress-strain curves for the unirradiated CuCrZr-alloy tested at different temperatures (a) before and (b) after single HIP at 960°C for 3 h. Note the decrease in tensile strength due to HIP-ing.

The joints were produced by HIP at 960°C for 3 hours at a pressure of 120 MPa followed by one hour furnace cooling and subsequent ageing treatment at 460°C for 2 hours for the CuCrZr alloy. Multiple thermal cycles were simulated by giving two additional heat treatments at 960°C for 3 hours followed by furnace cooling and subsequent heat treatment for CuCrZr HIP joint specimens at 460°C for 2 hours followed by furnace cooling.

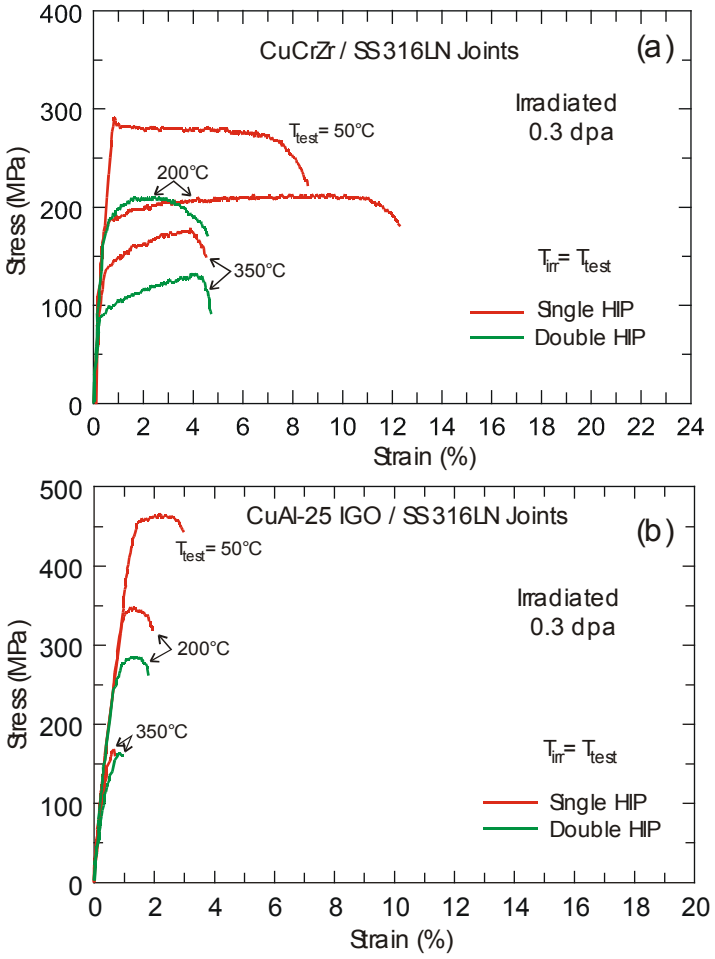

Figure 24. Stress-strain curves for joint specimens tensile tested at different temperatures after irradiation in the single and double HIP-ed conditions: (a) CuCrZr and (b) CuAl-25 joints with 316 austenitic stainless steel.

Tensile specimens were irradiated with fission neutrons in the DR-3 reactor at Risø at temperatures in the range of 50 – 350°C to a neutron fluence of 1.5 x 10^{24} n/m^2 (E > 1 MeV) corresponding to a displacement dose of 0.3 dpa (NRT). Irradiations at 200 and 350°C were carried out in a temperature controlled rig and in the atmosphere of helium or a mixture of helium and argon. Both unirradiated and irradiated specimens were tensile tested in vacuum and at the irradiation temperatures.

The results demonstrated that the tensile strength of HIP joint specimens of both copper alloys was considerably lower than that for the alloys without HIP treatment. This is illustrated in Figure 23 for CuCrZr alloy joints tested at different temperatures. In other words, the HIP treatment itself has a significant effect. This is further supported by the results showing that the double HIP thermal cycle reduced the strength even further of both alloys. In both copper alloy HIP joint specimens, the neutron irradiation induced a significant increase

in the yield strength but also a corresponding decrease in the uniform elongation. This is illustrated in Figure 24 for both alloys. Note that at the irradiation and test temperatures of 350°C, the joint specimen of CuAl-25 (IGO) has practically no ductility after irradiation.

3.2.3 Effect of neutron irradiation on fracture toughness behaviour of HIP joints copper alloys and 316 (LN) stainless steel

S. Tähtinen (*VTT Manufacturing Technology, Finland), B.N. Singh and P. Toft*

The work reported in this section compliments the results reported in the previous section (3.2.2) on the tensile properties of joints of copper alloys with stainless steel. The same materials, joining procedure and multiple HIP thermal heat treatments as described in section 3.2.2 were used in the present work. Three point bend test joint specimens of CuAl-25 (IGO) and CuCrZr (Outokumpu OY) with austenitic stainless steel 316 (LN) IG (of dimensions 3 x 4 x 27 mm^3) were used for fracture toughness testing before and after irradiation at different temperatures.

The fracture toughness specimens were irradiated with fission neutrons in the DR-3 reactor at Risø at temperatures in the range of 50 – 350°C to a neutron fluence of 1.5 x 10^{24} n/m^2 (E > 1 MeV) corresponding to a displacement dose of 0.3 dpa (NRT). Irradiations were carried out with a neutron flux of 2.5 x 10^{17} n/m^2s (E > 1 MeV) corresponding to a damage rate of 5x10^{-8} dpa/s (NRT). Irradiations were performed in the atmosphere of helium or a mixture of helium and argon. Irradiations at 200 and 350°C were carried out in a temperature controlled rig.

All bend test specimens were pre-cracked to the initial crack length to specimen width ratio of about 0.5 and 20% side grooved. The fracture resistance curves were determined for unirradiated as well as irradiated specimens at temperatures in the range of 22 – 350°C in a silicon oil bath following the ASTM E 1737-96 standard procedure.

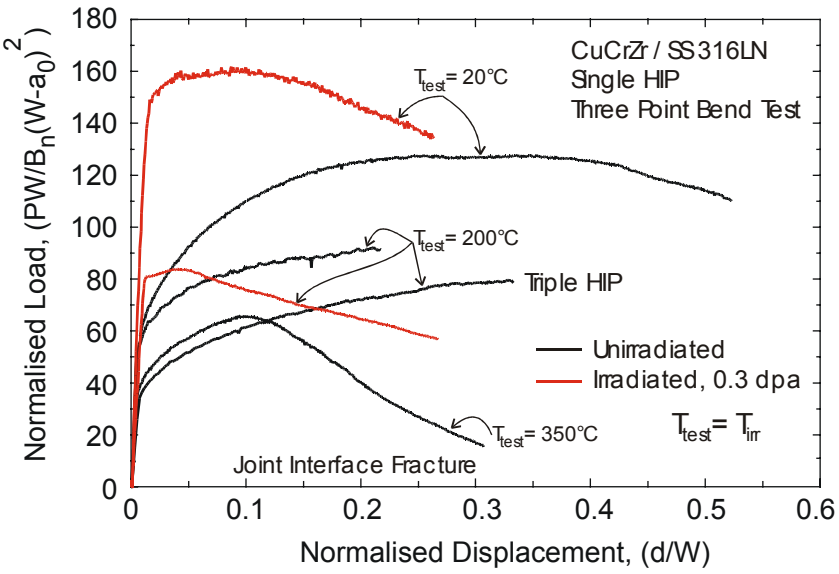

Figure 25. Normalised load and load displacement curves for single HIP joint specimens of CuCrZr-alloy with 316 austenitic stainless steel in the unirradiated and neutron irradiated conditions at different temperatures.

Figure 25 and Figure 26 illustrate the normalised load and load line displacement curves of single and triple HIP joint specimens of CuCrZr and CuAl25 IGO alloys with stainless steel in unirradiated and neutron irradiated conditions at different test temperatures. The observed displacement values at maximum loads were about an order of magnitude smaller in CuAl25 IGO alloys compared to that in CuCrZr alloy HIP joint specimens. In CuCrZr alloy HIP joints the crack deviated from the joint interface and propagated in the CuCrZr matrix at temperatures below 200°C. The fracture mode changed to joint interface, along the zirconium carbonitride layer, in both single and triple HIP CuCrZr alloy joint specimens at 350°C. In single HIP CuAl25 IGO alloy joints crack propagated in copper matrix close and parallel to HIP joint interface at all test temperatures. After triple HIP thermal cycle, the fracture mode changed to joint interface fracture. The multiple HIP joint specimens showed consistently lower load values in both copper alloys HIP joints when compared with single HIP joint specimens.

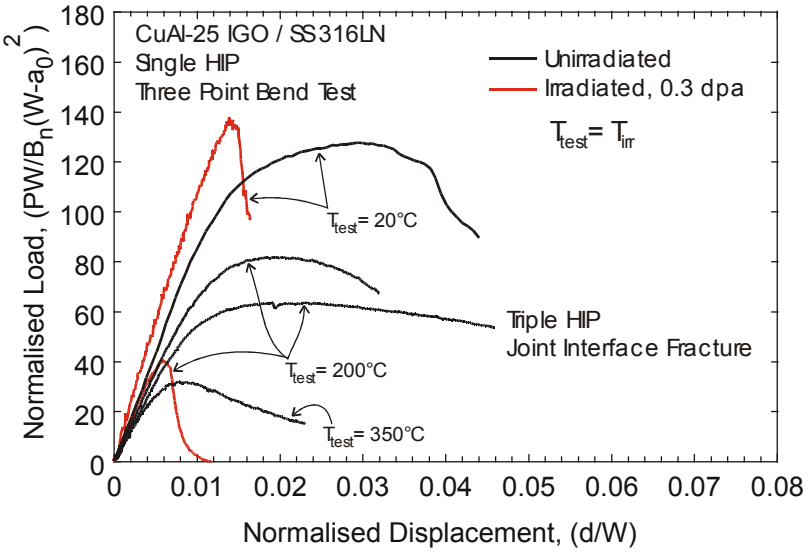

Figure 26. Normalised load and load displacement curves for single HIP joint specimens of CuAl-25 (IGO)-alloy with 316 austenitic stainless steel in the unirradiated and neutron irradiated conditions at different temperatures.

The effect of neutron irradiation on the normalised load and load line displacement curves of single HIP CuCrZr alloy joints showed significant hardening and lower displacement values at maximum load at temperatures below 200°C when compared with those in irradiated condition. In the CuAl25 IGO alloy HIP joints the measured loads and displacements after neutron irradiation were lower than those in the unirradiated condition. The corresponding fracture toughness of CuAl25 IGO alloy HIP joints were an order of magnitude lower than that of CuCrZr alloy HIP joints both in unirradiated and neutron irradiated conditions.

Multiple HIP thermal cycles enhanced the diffusion of elements across the HIP joint interface between CuCrZr as well as CuAl-25 IGO alloys with stainless steel. This led to phase transformations, precipitation, porosity formation and migration of the joint interfaces. In the three point bend tests, at 350°C the fracture mode in the single and triple HIP CuCrZr alloy changed to interface fracture. In the case of the triple HIP CuAl-25 IGO joints, the interface fracture occurred at temperatures above 200°C. The fracture behaviour of HIP joint

specimens were dominated by the strength mismatch between the base alloys (i.e. copper alloys and stainless steel.

3.2.4 Microstructure and mechanical properties of unirradiated and neutron-irradiated titanium alloys

B.N. Singh, P. Toft and D.J. Edwards (* Pacific Northwest National Laboratory, Richland, USA)*

The (α+β) titanium alloy (Ti-6Al-4V) was selected as a candidate material for flexible connectors between the blanket modules and the backplate of ITER. In view of an almost complete lack of knowledge about the effect of irradiation on microstructural evolution and mechanical properties, the present investigation were initiated to evaluate the response of this alloy to neutron exposure at 50 and 350ºC. For comparison, also the α-titanium alloy (Ti-5Al-2.5Sn) was included.

Both tensile and fatigue specimens of α an (α+β) alloys were irradiated at ~50 and 350ºC with fission neutrons in the DR-3 reactor at Risø to a fluence level of 1.5×10^{24} n/m^2 (E>1 MeV) corresponding to a displacement dose of about 0.3 dpa (NRT). All irradiations were carried out with a neutron flux of 2.5×10^{17} n/m^{2}s (E>1 MeV) corresponding to a damage rate of ~5×10^{-8}dpa/s. Both unirradiated and irradiated specimens were tensile rested in vacuum at temperatures equal to the irradiation temperatures. The microstructures of the as-supplied material and tensile tested (unirradiated) specimens were investigated using transmission electron microscopy. Fracture surfaces of the tensile tested (unirradiated) specimens were examined using scanning electron microscopy.

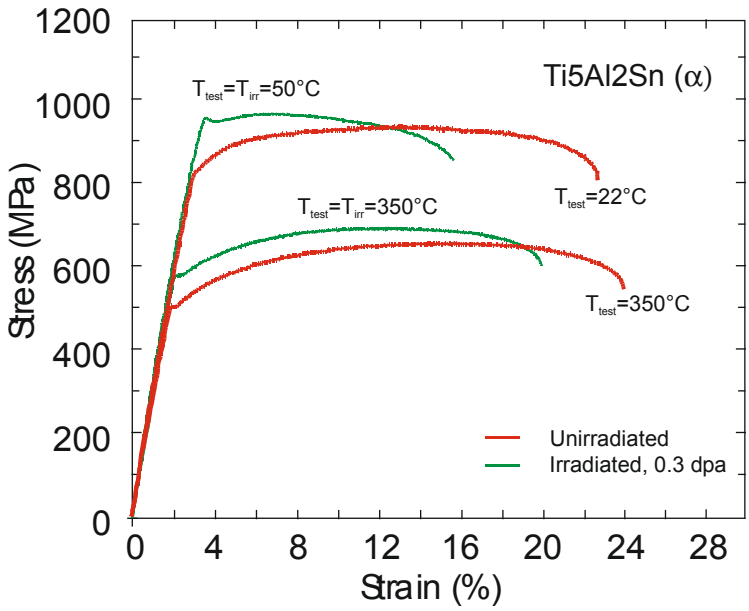

Figure 27. Stress-strain curves for α-Ti-alloy tested at different temperatures in the unirradiated and irradiated conditions.

The tensile behaviour of both alloys in the unirradiated condition has been reported earlier. Figure 27 and Figure 28 show the stress-strain curves for the irradiated alloys at 50 and 350ºC. For comparison, the corresponding curves for the unirradiated specimens are also included. It can be seen that in the case of the α-alloy, the magnitude of irradiation-induced hardening is rather small at both irradiation temperatures. However, it is quite clear that this material shows tendency to become plastically unstable in the irradiated condition, particularly at 50ºC. In the case of (α+β) alloy, the irradiation-induced hardening at 50ºC is also rather small. However, there is a significant decrease in the uniform elongation after irradiation. It is also noteworthy that the irradiation at 350ºC causes a very substantial amount of hardening in (α+β) alloy but only a modest decrease in the uniform elongation.

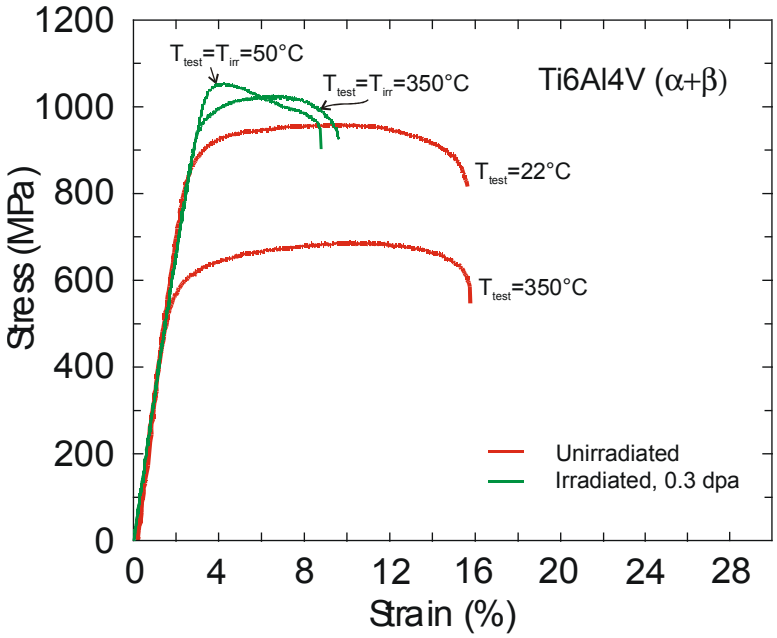

Figure 28. Stress-strain curves for **(α+β)** Ti-alloy tested at different temperatures in the unirradiated and irradiated conditions.

The unirradiated specimens of both α and (α+β) alloy were fatigue tested in the as-supplied condition at 50ºC. Fatigue testes were conducted in vacuum and in a strain controlled mode with fully reversed cycles (i.e. R=-1). The loading frequency was 0.5 Hz. The specimens were cycled to failure. The fatigue life (number of cycles to failure) is shown in Figure 29 as a function of the total strain range. As it can be seen, for both alloys, the number of cycles to failure increased with decreasing strain amplitude. The results also show that the fatigue behaviour of the two alloys is very similar.

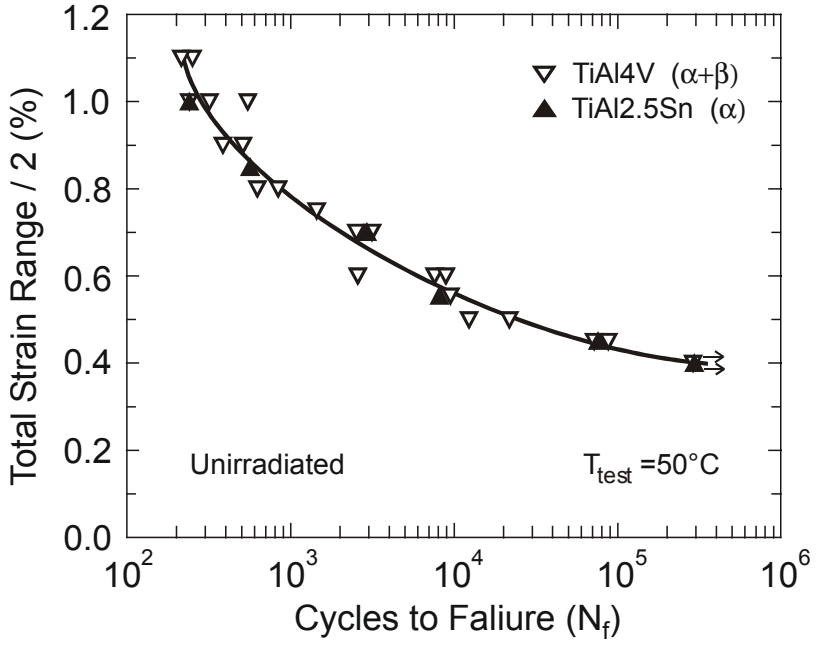

Figure 29. Fatigue life (N_f) as a function of total strain range for α and (α+β) Ti-alloys tested in the unirradiated condition at 50°C.

3.3 Long Term Technology

3.3.1 Annealing behaviour of irradiation-induced defects in pure iron

M. Eldrup and B.N. Singh

The problem of void formation in bcc metals and alloys (in particular steels) has been the subject of investigations in a number of laboratories. With the aim of obtaining a better understanding of these problems, such as the influence of irradiation temperature, annealing treatment and the presence of gas, a series of experiments on pure iron as well as F82H steel (next section) have been initiated.

To study the annealing behaviour of pure iron after neutron irradiation, positron annihilation spectroscopy (PAS) and electrical conductivity measurements have been applied together with transmission electron microscopy (TEM). PAS has the advantage that it is sensitive to vacancy-type defects such as single vacancies, two-dimensional vacancy clusters (i.e. loops) and three-dimensional vacancy agglomerates (i.e. voids and gas bubbles). With PAS it is possible to detect sub-microscopic voids and get information about their sizes, since the lifetime of positrons that are trapped in such sub-microscopic voids will increase with their size in the range from mono-vacancies up to agglomerates of about 50 vacancies. In addition, the technique provides information about the density of such cavities.

For comparison with the annealing behaviour of iron that had been neutron irradiated at 100°C (reported earlier) specimens of pure iron were neutron irradiated at 50°C in the DR-3 reactor at Risø to a displacement dose level of 0.23 dpa. As reported previously, electrical conductivity measurements show a big difference between specimens irradiated at 50° and at

100°C. This difference was associated with the trapping of vacancies by impurity carbon atoms that are immobile below ~70°C. In contrast to the conductivity data, the PAS results for specimens irradiated at 50° and at 100°C are very similar, both for the as-irradiated state and during the annealing treatment. The results show that in the as-irradiated specimens a high density (~10^{24} m^{-3}) of micro-voids containing 10 - 15 vacancies are present. On annealing, the density of micro-voids decreases above ~100°C while that for voids (of ~1 nm or larger diameter) increases to a maximum at about 250°C and then decreases to the detection level at ~400°C. This coarsening of micro-voids and voids was also reflected in the electrical conductivity of the specimens (see Figure 30).

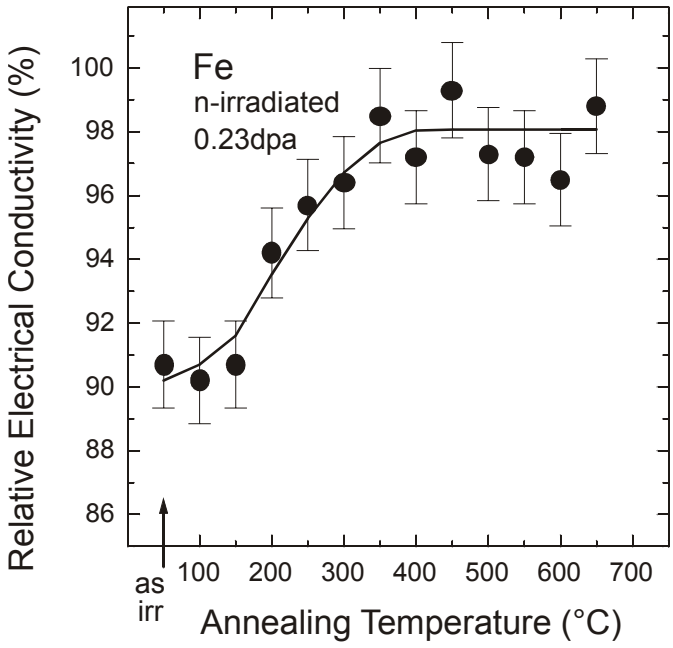

Figure 30. Relative electrical conductivity for irradiated iron as a function of annealing temperature (100% is equivalent to un-irradiated iron). The coarsening of micro-voids and voids is reflected in the increase of the conductivity.

Specimens for TEM were also prepared and annealed to the various temperatures. The TEM investigations confirmed that voids developed during annealing.

3.3.2 Investigation of cavity formation in pure iron and F82H steel

M. Eldrup and B.N. Singh

There has been some uncertainty as to the presence of voids in F82H steel after irradiation due to apparently conflicting experimental results. In order to try to contribute to a clarification of this problem positron annihilation spectroscopy (PAS) has been applied to search for voids and micro-voids in F82H after neutron irradiation and, for comparison, in irradiated pure iron. As mentioned above PAS is sensitive to the presence of three-dimensional vacancy agglomerates in the size range from mono-vacancies to voids as well as to vacancy loops etc.

Specimens of F82H were neutron irradiated in the DR-3 reactor at Risø to a displacement dose level of 0.23 dpa (equivalent to a fluence level of 1.5×10^{24} n/m^2) at the temperatures of

50, 250 and 350°C. Similarly, specimens of pure iron were irradiated to the same dose level at 50, 100, 200 and 350°C.

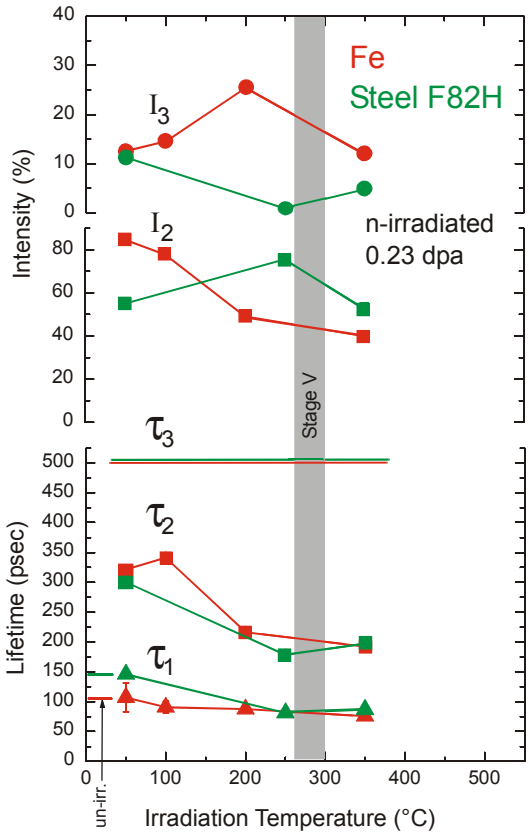

Figure 31. Positron lifetimes and their intensities as functions of irradiation temperature for Fe (red) and F82H steel (green). At low temperatures (50 and 100°C) both voids (τ_3 = 500 ps, I_3) and micro-voids (τ_2 ~ 330 ps, I_2) are formed, while at higher temperatures no micro-voids are seen. In the steel the void density is appreciably lower than in iron, and lower at 250°C than at the two other irradiation temperatures.

The PAS results (see Figure 31) show that in both F82H and iron voids are formed during neutron irradiation in the whole temperature range investigated. In addition, at the lower irradiation temperatures also micro-voids are formed in both materials. The highest density of voids in iron is obtained for the 200°C irradiation, while in the steel, the void density has its lowest value after irradiation at 250°C. At both 250°C and 350°C the void density in the steel is appreciably lower than in iron.

Thus, the measurements confirm that voids are indeed formed in F82H although with lower densities than in iron.

3.3.3 Study of loop-dislocation interaction in bcc iron

Yu.N. Osetsky, D.J. Bacon*, F. Gao* (*)University of Liverpool, Liverpool, England), A. Serra** (**)Polytechnical University, Barcelona, Spain) and B.N. Singh*

One of the important consequences of the one dimensional glide of clusters of self-interstitial atoms (SIAs) produced in cascades during neutron irradiation is the creation of specific microstructure features such as decoration of dislocations by small SIA loops[1)] and formation of rafts of dislocation loops[2)]. These observation formed the basis for the formulation of the

cascade-induced source hardening (CISH) model[3] for explaining the commonly observed radiation hardening and low-temperature embrittlement. While calculating the predictions of the CISH model, it was necessary to use the linear elasticity theory for determining the strength of loop-loop and dislocation-loop interactions. However, it is not known with complete confidence as to whether or not these "close-distance" interactions can be calculated accurately enough within the framework of elasticity theory. It was therefore decided to eliminate this uncertainty by calculating the strength of these interactions using atomic scale simulations.

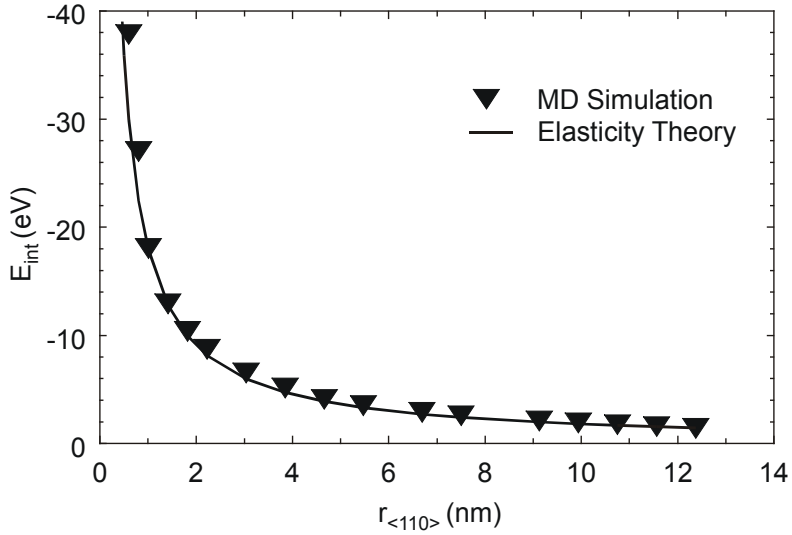

Figure 32. Interaction Energy of a 37-SIA loop with an edge dislocation as a function of distance between the dislocation line and the loop centre, $r_{<110>}$, below the extra half-plane.

Molecular statics (MS) was used to study energy of loop-loop and loop-dislocation interactions at zero temperature in crystallites containing np to 2.2×10^5 mobile atoms. An edge dislocation with $\underline{b} = \frac{1}{2} \langle 111 \rangle$ along line direction $[11\bar{2}]$ was created initially and then relaxed. A loop of a given size with the same Burgers vector as the edge dislocation was then created in the same plane at a given distance $r_{<110>}$ (from the edge dislocation) along $[1\bar{1}0]$ direction, i.e. below the extra half-plane of the edge dislocation, and the crystallite was relaxed again. Following this procedure, the interaction energy, E_{int}, was obtained for an interstitial loop containing 27 atoms as a function of distance between the dislocation line and the loop centre (see Figure 12). For comparison, the loop-dislocation interaction energy was calculated using elasticity theory for an isotropic medium (full line in Figure 32). It can be seen that even the simple isotropic elasticity theory seems to describe the loop-dislocation interaction quite well for distances between a loop and an edge dislocation down to 1nm. This is very encouraging since this distance is smaller than the "stand off" distance in the CISH model (in the CISH model, all loops within the stand off distance are assumed to be absorbed by the dislocation). In other word, the strength of interaction and hence the level of hardening calculated within the framework of CISH model appears to be reasonably realistic.

1. B.N. Singh, A. Horsewell, P. Toft and D.J. Edwards, J. Nucl.Mater. 224 (1995) 131.
2. B.N. Singh, J.H. Evans, A. Horsewell, P. Toft and G.V. Müller, J. Nucl.Mater. 256-263 (1998) 865.
3. B.N. Singh, A.J.E. Foreman and H. Trinkaus, J. Nucl.Mater. 251 (1997) 103.

3.4 Underlying Technology

3.4.1 Effects of Burgers vector changes on the reaction kinetic of gliding interstitial cluster

H.L. Heinisch (*PNNL, Richland, USA), B.N. Singh and S.I. Golubov*

Recently, it was demonstrated that there are significant differences in the defect accumulation behaviour between fcc and bcc metals irradiated under cascade damage conditions over a wide temperature range. [1)] While addressing this problem, it was recognised that the treatment of the damage accumulation within the framework of the production bias model (PBM) must include the effects of changes in the Burgers vector of SIA clusters during their one-dimensional (1-D) diffusional transport. This required that a new type of defect reaction kinetics had to be investigated since the reaction kinetics is expected to change with the frequency of changes in the Burgers vectors. Since there existed no rigorous mathematical description of the reaction kinetics for 1-D diffusion with random changes in the direction of diffusion, it was decided to investigate this problem using kinetics Monte Carlo computer simulations.

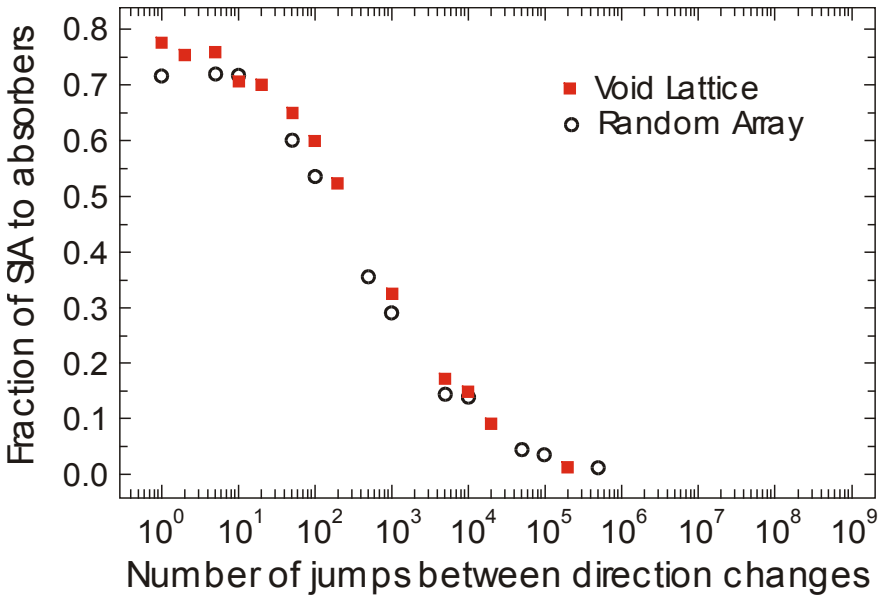

Figure 33. The fraction of migrating SIA absorbed as a function of the average distance, L, between direction changes for a periodic and a random array of absorbers of radius R=0.9 nm and concentration $C=4x10^{22}$ m^{-3}.

In the present work, the simulations have investigated the changes in reaction kinetics of 1-D migration of SIA clusters produced in cascades in copper as a function of changes in the Burgers vector and variation in the size and density of randomly or periodically distributed sinks. The effect of variation of the average distance travelled between Burgers vector changes, L, on the absorption of individual defect clusters into absorbers of varying sizes and varying concentrations were investigated. The effect of variation in L on the time dependence of absorption of a collection of defect clusters into an array of absorbers were also studied. The results clearly demonstrated that changes in Burgers vector of 1-D diffusion interstitial clusters has significant effects on the reaction kinetics (an example is shown in Figure 33).

Thus, the simulation results support the proposal that when evaluating the problem of damage accumulation under cascade damage conditions it is necessary to consider the effect of changes in the Burgers vector of the sinks in the crystal.

1. B.N. Singh and J.H. Evans, J. Nucl.Mater. 226 (1995) 277.

3.4.2 Damage accumulation in Cu-Ni alloys during neutron irradiation

S.J. Zinkle (*) ORNL, Oak Ridge, USA) and B.N. Singh*

For a number of years, Cu-Ni binary alloys have been considered to be suitable materials to study the effect of solute elements on damage accumulation during irradiation. The main argument for these studies has been that a proper understanding of the mechanisms in these simple alloys may help understand and hopefully predict the swelling behaviour in more complicated commercial alloys. A detailed and systematic investigation of the swelling behaviour of these alloys using 1 MeV electrons was made already some years ago[1]. However, the damage production during neutron irradiation is likely to occur in the form of cascades and not Frenkel pairs as in the case of 1 MeV electron irradiation. According to the production bias model, the damage accumulation under neutron irradiations should be significantly different from that under 1 MeV electron irradiation. In order to verify this proposition, it was decided to investigate the damage accumulation behaviour in Cu-Ni alloys.

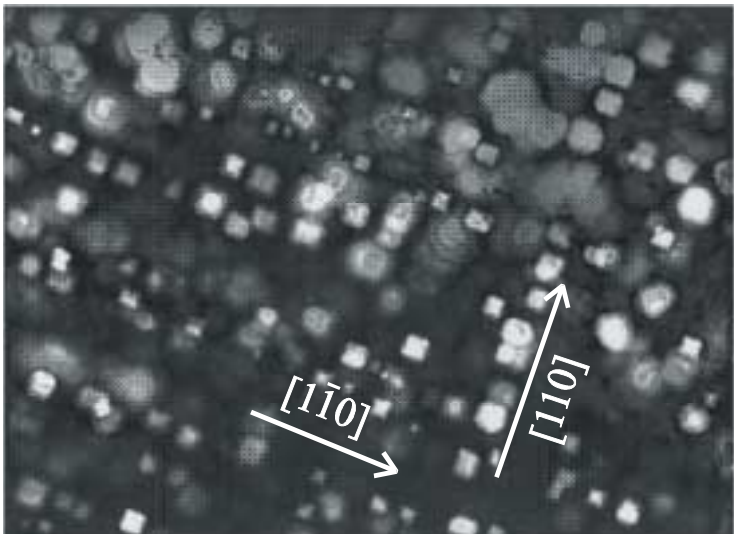

Figure 34. Partial void ordering along <110> crystallographic directions in Cu-10% Ni irradiated with fission neutrons to 14.9 dpa at 420°C.

Transmission electron microscope (TEM) disks of pure copper containing 0.17-10% Ni were neutron irradiated at 210 and 420ºC in Hf-shielded capsules in the High Flux Isotopes Reactor to doses of 13.5 and 14.9 displacements per atom (dpa), respectively. Void swelling was not observed in any of the specimens irradiated at 210ºC. Instead, a high density of stacking fault tetrahedra (SFTs) and a moderate density of dislocation loops were observed. There was no evidence for defect cluster patterning (wall formation) in any of the specimens irradiated at 210ºC, which suggests that patterning is not a fundamental self-organization phenomenon in neutron-irradiated copper. The SFT density was independent of Ni content, whereas the loop density was highest in the alloy containing ~2% Ni. Pronounced void swelling was observed in all of the specimens irradiated at 420ºC. A void denuded zone of

~2μm width was observed adjacent to grain boundaries. The void swelling in copper containing ~2% Ni showed a pronounced maximum in a 10μm wide band adjacent to the grain boundary denuded zones. Void swelling was very low in the middle of the grains in these specimens. Matrix voids aligned along <110> directions were observed in Cu-10% Ni irradiated at 420ºC (see Figure 34). The occurrence of the peak swelling zone and the partial ordering of voids are both consistent with the predictions of the recent production bias model which includes 1-D diffusional transport of clusters of self interstitial atoms.

1. B.N. Singh, T. Leffers and P. Barlow, in: Proc. 5th Intern. Conf. on High voltage Electron Microscopy, Kyoto (Japanese Soc. of Electron Microscopy, Tokyo, 1977) p. 581.

3.4.3 Effect of temperature on void formation in copper and Cu-Ni alloys

M. Eldrup and B.N. Singh

In bcc metals and alloys void formation apparently takes place during neutron irradiation in a wide temperature range below stage V. This does not seem to be the case in fcc metals. In order to take advantage of the sensitivity to micro-voids of the positron annihilation spectroscopy (PAS), it was decided to carry out PAS measurements on copper specimens that had been neutron irradiated at temperatures in the range of 50 to 350°C to look for the possible formation of micro-voids (and voids). In all cases the specimens were irradiated to a displacement dose level of 0.3 dpa in the DR-3 reactor at Risø.

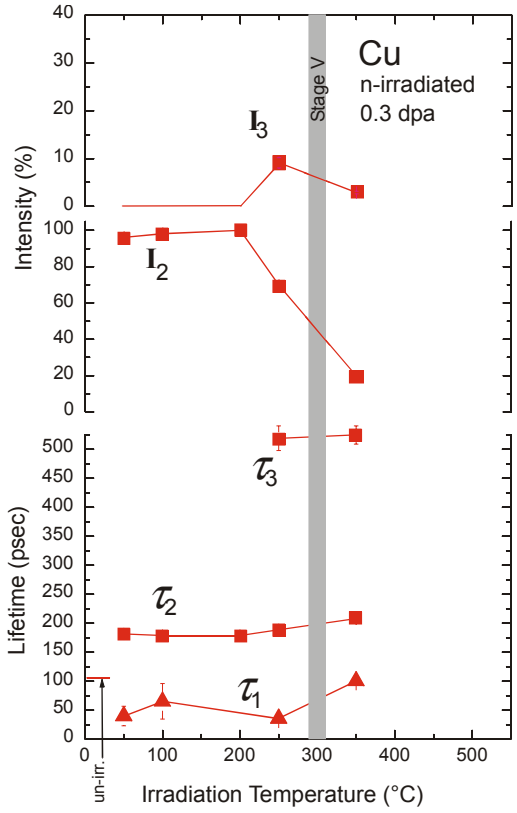

Figure 35. Positron lifetimes and their intensities plotted as functions of irradiation temperature for Cu. At low temperatures the dominating defect lifetime is τ_2 ~180 ps which may be associated with vacancies, dislocation loops or stacking fault tetrahedra. Above ~200°C the density of these defects decreases, as indicated by the decrease of I_2, and voids develop, as seen by the presence of the long-lived τ_3, I_3 component.

The results show (see Figure 35) that for irradiation temperatures at 200°C and below, no micro-voids can be observed, while at 250 and 350°C the formation of voids is clearly seen. In comparison, PAS measurements of Cu-Ni alloys with 2 and 5 % Ni, irradiated to 0.3 dpa at 350°C, give no indication of void formation (which may be contrasted to the void swelling observed after irradiation at 420°C to a high dose (see section 3.4.2)).

The copper specimen that was irradiated at 100°C was subsequently annealed to 650°C in steps of 50°C. No changes were observed in the positron parameters below 300°C (stage V). Above this temperature, however, a strong decrease of the density of the detected defects (small, gas stabilised vacancy clusters and maybe SFTs) takes place. At temperatures higher than ~450°C a low density of micro-voids or bubbles can be detected.

3.5 Participants in Fusion Technology

3.5.1 Scientific staff

Eldrup, Morten	(part time ~70%)
Singh, B.N.	
Toft, Palle	(part time ~70%)

3.5.2 Technical staff

Lindbo, Jørgen	(part time ~20%)
Nilsson, Helmer	(part time ~10%)
Olsen, Benny F.	
Pedersen, N.J.	(part time ~40%)

3.5.3 Guest scientists

Edwards, D.J.
Pacific Northwest National Laboratory, Richland, USA
Zinkle, S.J.
Oak Ridge National Laboratory, Oak Ridge, USA
Stubbins, J.F.
University of Illinois, Urbana-Champaign, USA
Trinkaus, H.
Forschungszentrum Jülich, Jülich, Germany
Golubov, S.I.
Institute of Physics and Power Engineering, Obninsk, Russia

3.6 Publications and Conference Contributions

3.6.1 International publications

Heinisch, H.L.; Singh, B.N., Simulation of the kinetics of defect accumulation in copper under neutron irradiation. J. Nucl.Mater (1999) v. 271/272 p. 46-51

Heinisch, H.L.; Singh, B.N., A kinetic Monte Carlo study of mixed 1D/3D defect migration. J. Comput. –Aided Mater. Des. (1999) v. 6 p. 277-282

Heinisch, H.L.; Singh, B.N., Golubov, S.I., A kinetic Monte Carlo study of mixed 1-D/3-D defect migration. In: Fusion Materials. Semiannual progress report for the period ending June 30, 1999. DOE/ER-0313/26 (1999) p. 179-183

Singh, B.N., Atomic displacements and defect accumulation during irradiation with energetic particles: An autobiographical review. Radiat. Eff. Defects Solids (1999) v. 148 p. 383-446

Singh, B.N., Damage production, accumulation and materials performance in radiation environment. J. Comput. –Aided Mater.Des. (1999) v. 6 p. 195-214

Singh, B.N.; Horseweel, A; Toft, P., Effects of neutron irradiation on microstructure and mechanical properties of pure iron. J. Nucl.Mater. (1999) v. 271/272 p. 97-101

Singh, B.N.; Stubbins, J.F.; Toft, P., The influence of neutron irradiation on the fatigue performance of OFHC copper and a dispersion strengthened copper alloy. J. Nucl.Mater. (1999) v. 275 p. 125-137

3.6.2 Danish reports

Lynov, J.P.; Singh, B.N. (eds.), Association Euratom – Risø National Laboratory annual progress report for 1998. Risø-R-1136(EN) (1999) 46p.

3.6.3 Foreign books and reports

Edwards, D.J.; Singh, B.N.; Toft, P. Eldrup, M., Post-irradiation annealing response of pure copper irradiated at 100 deg.C. In: Fusion materials. Semiannual progress report for the period ending June 30, 1999. DOE/ER-0313/26 (1999) p. 121-125

Heinisch, H.L.; Singh, B.N.; Golubov, S.I., Kinetic Monte Carlo studies of the effect of one-dimensional glide on the reaction kinetics of interstitial cluster. In: Fusion materials. Semiannual progress report for the period ending December 31, 1998. DOE/ER-0313/25 (1999) p. 271-274

3.6.4 Conference proceedings

Ghoniem, N.M.; Singh, B.N., Dislocation dynamics study of the onset of plastic instabilities in irradiated materials. In: Deformation-induced microstructures: Analysis and relation to properties. Proceeding. 20. Risø international symposium on materials science, Risø (DK), 6-10 Sep 1999. Bilde-Sørensen, J.B.; Carstensen, J.V.; Hansen, N.; Juul Jensen, D.; Leffers, T.; Pantleon, W.; Pedersen, O.B.; Winther, G. (eds.), (Risø National Laboratory, Roskilde, 1999) p. 41

3.6.5 Unpublished lectures

Eldrup, M.; Singh, B.N., A comparison of neutron irradiated copper and iron: Effects of irradiation and annealing.9. International conference on fusion reactor materials (ICFRM 9), Colorado Springs, CO (US), 10-15 Oct 1999.

Heinisch, H.L.; Singh, B.N.; Golubov, S.I., The effects of one-dimensional glide of interstitial defects accumulation under fusion neutron irradiation. 9. International conference on fusion reactor materials (ICFRM 9), Colorado Springs, Co (US), 10-15 Oct 1999. Unpublished.

Hirade, T.; Maurer, F.H.J.; Eldrup, M., Positronium formation at low temperatures: The role of trapped electrons. 6. International workshop on positron and positronium chemistry (PPC 6), Tsukuba (JP), 6-11 Jun 1999. Unpublished.

Osetsky, Y.N.; Bacon, D.J.; Gao, F.; Serra, A.; Singh, B.N., Study of loop-loop and loop-edge dislocation interactions in bcc iron. 9. International conference on fusion reactor materials (ICFRM 9), Colorado Springs, CO (US), 10-15 Oct 1999. Unpublished.

Singh, B.N., Consequences of defect production and accumulation during irradiation of crystalline solids: Progress and perspectives. Meeting at Indira Gandhi Centre for Atomic Research, Kalpakkam (IN), 25 Jan 1999. Unpublished.

Singh, B.N., Influence of damage production and accumulation on the bulk behaviour of metals and alloys. Workshop on damage production and accumulation, Liverpool (GB), 19-21 Aug 1999. Unpublished.

Singh, B.N., Response of crystalline solids to radiation with energetic projectiles. Meeting at Pacific Northwest National Laboratory, Richland, WA (US), 21 Oct 1999. Unpublished.

Singh, B.N., Status report on tensile, fatigue and microstructural investigations of titanium alloys before and after irradiation. EUHT expert meeting on materials tasks for ITER, Garching (DE), 9-10 Nov 1999. Unpublished.

Singh, B.N., Recent results of tensile, fatigue and microstructural investigations of copper alloys and their joints with stainless steel. EUHT expert meeting on materials tasks for ITER, Garching (DE), 9-10 Nov 1999. Unpublished.

Singh, B.N.; Edwards, D.J.; Toft, P., Influence of post-irradiation annealing on neutron irradiated OFHC copper: Changes in microstructure and mechanical properties. 9. International conference on fusion reactor materials (ICFRM 9), Colorado Springs, CO (US), 10-15 Oct 1999. Unpublished.

Singh, B.N.; Stubbins, J.F.; Toft, P., Effect of neutron irradiation on low cycle fatigue behaviour of CuAl-25 and CuCrZr alloys at 250 and 350 deg.C. 9. International conference on fusion reactor materials (ICFRM 9), Colorado Springs, CO (US), 10-15 Oct 1999. Unpublished

Sun, L.Z.; Ghoniem, N.M.; Singh, B.N., 3-D dislocation dynamics study of plastic instability in irradiated copper. 9. International conference on fusion reactor materials (ICFRM 9), Colorado Springs, CO (US), 10-15 Oct 1999. Unpublished.

Trinkaus, H.; Singh, B.N.; Golubov, S.I., Progress in modelling the microstructural evolution in metals under cascade damage conditions. 9. International conference on fusion reactor materials (ICFRM 9), Colorado Springs, CO (US), 10-15 Oct 1999. Unpublished.

Tähtinen, S.; Laukkanen, A.; Singh, B.N., Damage mechanisms and fracture toughness and Glid Cop Al25 copper alloys. 9. International conference on fusion reactor materials (ICFRM 9), Colorado Springs, CO (US), 10-15 Oct 1999. Unpublished.

Tähtinen, S.; Singh, B.N.; Toft, P., Effect of neutron irradiation on mechanical properties of Cu/SS joints after several HIP cycles. 9. International conference on fusion reactor materials (ICFRM 9), Colorado Springs, CO (US), 10-15 Oct 1999. Unpublished.

Zinkle, S.J.; Singh, B.N., Microstructure of copper alloys neutron irradiated at 200 and 400 deg.C. to 13 dpa. 9. International conference on fusion reactor materials (ICFRM 9), Colorado Springs, CO (US), 10-15 Oct 1999. Unpublished.

Bibliographic Data Sheet **Risø-R-1245(EN)**

Title and authors

Association Euratom – Risø National Laboratory
Annual Progress Report for 1999

Edited by J.P. Lynov and B.N. Singh

ISBN	ISSN
87-550-2834-9 87-550-2835-7 (Internet)	0106-2840

Department or group	Date
Optics and Fluid Dynamics Department	January 2001

Pages	Tables	Illustrations	References
50		35	18

Abstract (max. 2000 characters)

The programme of the Research Unit of the Fusion Association Euratom - Risø National Laboratory covers work in fusion plasma physics and in fusion technology. The fusion plasma physics group has activities within development of laser diagnostics for fusion plasmas and studies of nonlinear dynamical processes related to electrostatic turbulence and turbulent transport in magnetised plasmas. The activities in technology cover investigations of radiation damage of fusion reactor materials. These activities contribute to the Next Step, the Long-term and the Underlying Fusion Technology programme. A summary is presented of the results obtained in the Research Unit during 1999.

Descriptors INIS/EDB

LASER DOPPLER ANEMOMETERS; MAGNETIC CONFINEMENT; NONLINEAR PROBLEMS; NUMERICAL SOLUTION; PELLET INJECTION; PHYSICAL RADIATION EFFECTS; PLASMA DIAGNOSTICS; PLASMA SCRAPE-OFF LAYER; PLASMA SIMULATION; PROGRESS REPORT; RISOE NATIONAL LABORATORY; THERMONUCLEAR REACTOR MATERIALS; TOKAMAK DEVICES; TURBULENCE; VORTICES

Available on request from Information Service Department, Risø National Laboratory,
(Afdelingen for Informationsservice, Forskningscenter Risø), P.O.Box 49, DK-4000 Roskilde, Denmark.
Telephone +45 4677 4004, Telefax +45 4677 4013, email: risoe@risoe.dk